Acta Biomaterialia 151 (2022) 426–445

Contents lists available at ScienceDirect

Acta Biomaterialia

journal homepage: www.elsevier.com/locate/actbio

Full length article

Equine hoof wall: Structure, properties, and bioinspired designs

Benjamin S. Lazarus[a,*], Rachel K. Luu[b], Samuel Ruiz-Pérez[c], Wendell Bruno Almeida Bezerra[d], Kevin Becerra-Santamaria[e], Victor Leung[a], Victor Hugo Lopez Durazo[f], Iwona Jasiuk[g], Josiane D.V. Barbosa[h], Marc A. Meyers[a,b,i]

[a] Materials Science and Engineering, University of California San Diego, 9500 Gilman Drive, La Jolla, CA 92093-0418, USA
[b] Department of Mechanical and Aerospace Engineering, University of California San Diego, USA
[c] Facultad de Ciencias, Universidad Nacional Autónoma de México, Mexico City, Mexico
[d] Department of Materials Science, Military Institute of Engineering-IME, Rio de Janeiro 22290270, Brazil
[e] Facultad de Ingeniería, Arquitectura y Diseño, Universidad Autónoma de Baja California, Mexicali, Mexico
[f] Departamento de Ciencias Químico-Biológicas, Universidad de Sonora, Hermosillo, Mexico
[g] Department of Mechanical Science and Engineering, University of Illinois Urbana-Champaign, Champaign, IL, USA
[h] Department of Materials, University Center SENAI CIMATEC, Salvador, Brazil
[i] Department of Nanoengineering, University of California San Diego, USA

ARTICLE INFO

Article history:
Received 29 April 2022
Revised 14 August 2022
Accepted 15 August 2022
Available online 20 August 2022

Keywords:
Composite
Bioinspiration
Multi-material additive manufacturing
Impact resistance
Energy absorbtion
Biological material
Equine hoof
Viscoelasticity

ABSTRACT

The horse hoof wall exhibits exceptional impact resistance and fracture control due to its unique hierarchical structure which contains tubular, lamellar, and gradient configurations. In this study, structural characterization of the hoof wall was performed revealing features previously unknown. Prominent among them are tubule bridges, which are imaged and quantified. The hydration-dependent viscoelasticity of the hoof wall is described by a simplified Maxwell-Weichert model with two characteristic relaxation times corresponding to nanoscale and mesoscale features. Creep and relaxation tests reveal that the specific hydration gradient in the hoof keratin likely leads to reduced internal stresses that arise from spatial stiffness variations. To better understand realistic impact modes for the hoof wall *in-vivo*, drop tower tests were executed on hoof wall samples. Fractography revealed that the hoof wall's reinforced tubular structure dominates at lower impact energies, while the intertubular lamellae are dominant at higher impact energies. Broken fibers were observed on the surface of the tubules after failure, suggesting that the physically intertwined nature of the tubule reinforcement and intertubular matrix improves the toughness of this natural fiber reinforced composite. The augmented understanding of the structure-mechanical property relationship in dynamic loading led to the design of additively manufactured bioinspired structures, which were evaluated in quasistatic and dynamic loadings. The inclusion of gradient structures and lamellae significantly reduced the damage sustained in drop tower tests, while tubules increased the energy absorption of samples tested in compact tension. The samples most similar to the hoof wall displayed remarkably consistent fracture control properties.

Statement of significance

The horse hoof wall, capable of withstanding large, repeated, dynamic loads, has been touted as a candidate for impact-resistant bioinspiration. However, our understanding of this biological material and its translation into engineered designs is incomplete. In this work, new features of the horse hoof wall are quantified and the hierarchical failure mechanisms of this remarkable material under near-natural loading conditions are uncovered. A model of the hoof wall's viscoelastic response, based on studies of other keratinous materials, was developed. The role of hydration, strain rate, and impact energy on the material's response were elucidated. Finally, multi-material 3D printed designs based on the hoof's

---

[*] Corresponding author.
E-mail address: bslazaru@eng.ucsd.edu (B.S. Lazarus).

https://doi.org/10.1016/j.actbio.2022.08.028

meso/microstructure were fabricated and exhibited advantageous energy absorption and fracture control relative to control samples.

1. Introduction

Naleway et al. [1] identified eight key design motifs that commonly occur in structural biological materials. These include suture, tubular, fibrous, layered, cellular, helical, overlapping, and gradient structures. Nearly all of these structural elements are found in the horse hoof wall, which shows remarkable impact resistance and fracture control properties. These arrangements exist in a hierarchical assembly, meaning they are exhibited on multiple length scales. While nature's intricate hierarchical designs are still outside of engineers' grasp, these types of configurations often bear more finely tuned mechanical properties, such as improved energy absorption, higher toughness, and selective anisotropy [2]. The hoof wall also contains several other key design features that have proven vital for beneficial mechanical properties, including a composite nature, viscoelastic behavior, and unique porosity distributions.

The hierarchical structure of the equine hoof wall can be seen in Fig. 1. On the mesoscale, the hoof wall contains tubules that are approximately 40-100 μm in diameter [3]. The shape, size, and density of the tubules vary through the thickness of the hoof, gradually becoming more elliptical, smaller in cross-section, and more densely packed closer to the exterior of the hoof wall [4,5]. These tubules have a mostly hollow medullary cavity at the center, which is surrounded by a stiffer tubule wall. The wall is made of helical lamellae composed of thin pancake-shaped cells filled with nanoscale keratin intermediate filaments (IFs) [6,7]. The IFs are crystalline and act as fiber reinforcement for the hoof wall. Huang et al. [8] observed thin "bridges" within the medullary cavity but did not extensively study these structures. The tubules are embedded in a softer matrix composed of irregular, polygonal, keratin-filled cells [8]. These cells form lamellae that generally run orthogonally to the tubule axis but can also vary in orientation throughout the hoof wall [9]. The surfaces of the cells that compose these lamellae are sutured, providing increased mechanical stability through physical interlocking of the ridged interfaces. The hoof wall also contains a gradient in stiffness from the exterior of the hoof wall to the interior (near the living tissue) that arises from a hydration gradient, changes in reinforcement (from the tubule arrangement), and possibly variations in the IF density [5,9–11].

Multiple studies have explored the mechanical properties of the hoof wall and uncovered intriguing structure-property relationships. The tubules, with their anisotropic intertubular lamellae, have been reported to deflect cracks, increasing fracture toughness and providing the hoof a degree of crack path control [7,12]. Kasapi and Gosline [9,12] noted tubule pullout during tensile tests but suggest that crack deflection is the primary energy dissipative role of the tubules. Further, they postulate that IF orientation dominates crack propagation in the hoof wall and nearly always causes cracks to deviate away from the interior of the hoof, confirming the previous compact tension results of Bertram and Gosline [7]. Like other keratinous materials [8,11,13–20], the mechanical properties of the horse hoof are highly susceptible to hydration and strain rate. Bertram and Gosline [6] measured an approximately 36-fold increase in tensile elastic modulus between samples held in a 100% and 0% relative humidity environment. Kasapi and Gosline [12] observed a 3-fold increase in elastic modulus between tensile samples tested at a strain rate of 1.6 $\times$ 10^{-3} s^{-1} and 70 s^{-1}.

Despite the extensive research on the hoof wall's mechanical properties there are still numerous knowledge gaps. Many of the previous studies on the hoof wall's fracture control properties have focused on samples tested in tension [3,6,7,9,12]. While this can yield valuable results the primary loading mode of the hoof is in compression. Furthermore, nanoscale keratin experiences a transition from alpha helices to beta sheets when loaded in tension [21–24] but this has never been reported in compression. Of the studies that have utilized compressive tests, they have either been performed with a single cross-head speed [5,10] or used narrow or less precise hydration ranges [8,10]. Only two studies have explored the hoof's response to non-quasi-static strain rates. Kasapi and Gosline [12] used a compact tension arrangement with the cross-head attached to a pendulum to generate tensile strains of ~70 s^{-1}, while Huang et al. [8] used a split Hopkinson pressure bar to attain strain rates of ~1000 s^{-1}. Neither of these tests provide a realistic impact scenario for what the horse hoof would experience *in-vivo*.

Several researchers have designed engineered structures with enhanced mechanical properties based on the meso, sub-meso, and microscale (1 μm-1 mm) features of the hoof wall. Rice and Tan [25] performed single-edged notched bending tests on lamellar structures composed of epoxy and polylactic acid (PLA) and found that lamellar orientation can be tuned to improve stiffness and energy absorption during fracture. Wang et al. [26] fabricated 3D printed structures containing tubular arrangements and found that K_{IC} and G_{IC} increased by 39% and 55%, respectively, relative to control samples. Huang [27] used multi-material 3D printing to fabricate samples with four tubules each and found that they helped to prevent damage in comparison with featureless samples. Ma et al. [28] fabricated crashworthy structures inspired by the tubular and lamellar structures in hooves and used finite element analysis and experimental compression tests to determine that bioinspired samples absorbed significantly more energy when compressed. Hoof-inspired corrugated tubules exhibited a 94% increase in specific energy absorption over traditional square tubes while achieving a 66% decrease in the undulation of load-carrying capacity (a metric used to determine the smoothness of the force-displacement curve, where a lower value indicates a smoother curve). A lower undulation of load-carrying capacity suggests a more efficient deformation process.

In this study, we present new results on the structural characterization of the hoof wall, including measurements of the tubules, tubule bridges and their density, and the hierarchy of meso/microscale fibers in the hoof wall (Section 3.1). Expanding on the mechanical experiments of previous studies, compression tests at five different strain rates were performed on hoof samples hydrated to three different hydration levels. This wide range of testing conditions was used to capture the hydration and strain rate sensitivity of the hoof wall and to determine the ductile to brittle transition of this biological material. To determine the viscoelastic properties of the hoof wall, compressive creep and stress relaxation tests for different hydration levels were performed. The results are used to fit the hoof wall's response to a simplified Maxwell-Weichert model using a Prony series and are compared to another keratinous material, hair (Section 3.2). To supply an understanding of the hoof wall's

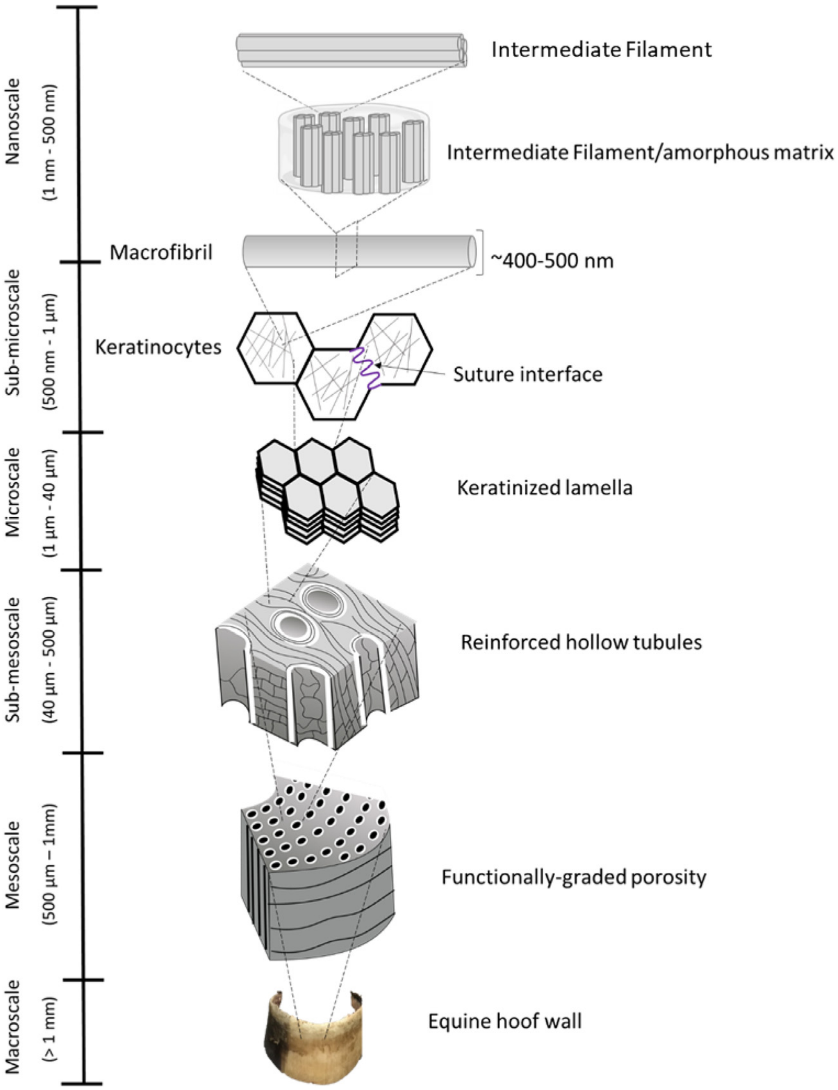

Fig. 1. The horse hoof wall exhibits a complex hierarchical structure. Each length scale contains its own characteristic design that contributes uniquely to the mechanical functionality of the bulk material. Figure adapted from [18].

fracture mechanics during a realistic impact, drop tower tests that closely resemble those experienced by the hoof wall *in-vivo* were performed and the resulting failure mechanisms are reported (Section 3.3). Based on these results and existing literature, unique multi-phase hoof-inspired structures were fabricated to show that elements of the hoof wall can be used to improve energy absorption and control crack propagation in engineered materials (Section 3.4).

2. Materials and methods

2.1. Hoof samples

Hoof samples were obtained from the University of California, Davis, Veterinary Department. They were taken from six racehorses of mixed age and gender that died due to musculoskeletal injuries. Each horse weighed between 450 and 550 kg. The hooves were removed from the corpse within 4-24 h and were then refrigerated for 24-48 h before being frozen at -20 °C. The keratinous hoof capsule was removed from the hoof before being cut down to the required sample dimensions. Hoof samples were taken from the central portion of the toe region. Two different methods were used to obtain desired hydration levels. The relative humidity method was used for the drop tower samples and involved placing samples in a sealed chamber with a desired relative humidity until the weight of the sample equilibrated. The water content by weight technique was used for compression samples. This method involved drying samples in an oven at 110 °C until their weight reached equilibrium. Samples were then placed in 70 °C water and periodically weighed until they reached the desired water content. Samples were tested immediately upon reaching the desired conditions. The relative humidity approach replicates better natural moisture conditions where water diffuses into a sample over an extended period of time at ambient temperatures. The water content approach is ideal for ensuring that all samples contain the same ratio of water. Since drop tower tests were intended to see how cracks propagate naturally in the hoof, relative humidity was chosen to modulate sample hydration. The compression tests, on the other hand, were meant to characterize the keratinous hoof wall at different moisture levels, so water content was chosen as a means of quantifying moisture in the hoof wall samples.

2.2. Bioinspired samples

Due to the promising mechanical performance of hooves reported by previous studies, bioinspired models were created to replicate the tubular, layered, and gradient structures found in the hoof. These different models aim to evaluate the mechanical properties and failure mechanisms imparted by its design motifs. Earlier studies have shown that the tubular structure in the hoof wall plays a vital role in its crack deflection mechanisms [3,9,12]. Thus, the tubular structure is of key interest for creating energy absorbent engineered materials. Models consisted of 64 tubules as a representation for the span of the hoof wall and focused on varying tubular shape gradients (elliptical to circular), density gradients (high density to low density), and the inclusion of soft intertubular lamellae. Dimensions of the tubules were drawn from Kasapi et al. [9] where the hoof stratum medium and externum were divided into six distinct regions. The average tubule shape, cavity size, and cross-sectional area reported for each region were scaled up enough to allow for 3D printing and replicated in the bioinspired models. Data for the density gradient comes from Reilly et al. [4]; it was adapted to fit 64 total tubules. For all models, the volume fraction of reinforced tubular area was held constant at 30% and the tubular cavity area at approximately 3% to match the values reported by Huang et al. [8]. Models were designed initially for drop tower impact testing to study the effect of structural features, both isolated and in varied combinations. A multi-material 3D printer (Objet350 Connex3, Stratasys, Rehovot, Israel) was used to fabricate the drop tower models, using polymers FLX9095-DM for the matrix, VeroClear for the reinforced tubules, and TangoBlack+ for the lamellae.

These bioinspired designs were adapted for compact tension experiments to explore how the various arrangements affected crack propagation. The designs were implemented into a modified Plastic ASTM D5045 – 14 specimen geometry (W=39.09 mm) with the tubules arranged orthogonal to the crack tip. The modifications consisted of re-positioning the pinholes for the sample to fit in the testing apparatus with enough clearance to avoid collision of the sample and the crosshead during ductile Mode I failure. The modification is not expected to have consequential effects on the results. The compact tension models consist of the same design but with the addition of two models; one which tests control (Model 1), composed of the stiff reinforcing tubular material and a model which has uniformly distributed tubules with an elliptical reinforcing region. For the latter, a shape ratio of 1.62 was chosen as this correlated to the most extreme elliptical tubules observed in the hoof by Kasapi et al. [9]. The intertubular lamellar designs were not studied in compact tension due to the prioritized focus of studying the effect of the tubular structure on crack propagation.

2.3. Microcomputed tomography

5 × 5 × 5 mm^3 cubes were removed from the hoof wall and scanned using an Xradia MicroXCT 200 (Zeiss, Jena, Germany). Two sets of scans were taken at different magnifications. A low magnification set was taken with an optical magnification of 3.9692 and a pixel size of 4.001 μm. These scans had an exposure time of 1.5 s, a voltage of 80 kV, and a current of 88 μA. Higher magnification scans were taken with an optical magnification of 19.312 and a pixel size of 1.1315 μm. These scans had an exposure time of 3 s, a voltage of 80 kV, and a current of 87 μA. The results were processed with Fiji/ImageJ (U. S. National Institutes of Health, Bethesda, Maryland, USA) [29] and 3D plugins [30,31] prior to measuring. The processing was customized based on the properties of the images, and consisted of brightness and contrast enhancements, noise reduction 3D filters, pixel thresholding, morphological 3D erosions and dilations, 3D hole filling, size-based object filtering, and object isolation from the stacks. Global 3D analysis of tubule morphology was conducted using the Volume Viewer plugin.

2.4. Compression tests

5 × 5 × 5 mm^3 samples taken from the hoof wall were tested using an Instron 3367 mechanical testing machine (Instron, High Wycombe, United Kingdom) with a 20 kN load cell. Despite bearing such large *in-vivo* loads, the hoof wall is only about 1 cm wide at its thickest, and this can vary between horses and even within the same hoof. The dimensions chosen for these tests were the largest possible ensuring that samples were composed exclusively of stratum medium (the central portion of the keratinized hoof wall). Samples were compressed in the longitudinal direction to 30% of their original height at three different hydration levels (10%, 20%, and 30% water content by weight) and five different strain rates (10^0 s^{-1}, 10^{-1} s^{-1}, 10^{-2} s^{-1}, 10^{-3} s^{-1} and 10^{-4} s^{-1}). Five samples were tested for each condition. Stress relaxation tests were also performed on 5 × 5 × 5 mm^3 samples at each hydration condition. These samples were compressed to 90% of their initial height at a strain rate of 10^{-1} s^{-1} before a 10 min relaxation period. Creep tests were conducted on samples of 20% and 30% water content. 5 × 5 × 5 mm^3 samples were compressed and held at a constant stress of 14.5 MPa (the average initial stress between the two hydrations for the stress-relaxation tests). The resultant change in strain was measured over a period of 700 s.

2.5. Drop tower tests

Drop tower impact testing was chosen as a characterization technique because it best recreates the natural localized impact that might be experienced by hoof when it lands on uneven terrain, such as a small rock, during locomotion. Hoof samples were tested in a drop tower specially made for testing biological samples described previously in detail [32]. For this study, the 1.2 kg impactor was raised to a height of 0.24, 0.48, and 0.72 m for impact energies of 2.8224, 5.6448, and 8.4672 J, respectively. Hoof samples were tested in two different hydration conditions of 25% and 50% relative humidity (RH). Five samples were tested for each impact energy at both hydration conditions. Samples were cut using a benchtop saw to be 17 × 8 × 3 mm^3.

Bioinspired samples were also characterized through drop tower testing. These tests were performed on a CEAST 9350 (Instron, High Wycombe, United Kingdom). The samples were impacted at 4 m/s ± 0.2 m/s by a 3.266 kg impactor (corresponding to ~26.1 J of impact energy) with a half-inch hemispherical tip. Force-displacement curves were measured, but no trends were observed for each type of sample, so they were not reported here. Instead, the analysis of these tests focused on the fracture surfaces and residual damage of impacted samples.

2.6. Fractography

Post-impact hoof samples were imaged using an FEI Apreo FE-SEM (Thermo Fisher Scientific, Waltham, Massachusetts, USA) after being sputter coated (Emitech K575X, Quorum Technologies Ltd, East Sussex, United Kingdom) with iridium for 8 s. Post-impact bioinspired samples were imaged using an Xradia microCT 200 (Zeiss, Jena, Germany). Scans were reconstructed and segmented in Amira 2020.2 (Thermo Fisher Scientific, Waltham, Massachusetts, USA) to obtain damage volume values.

2.7. Compact tension testing

Three samples of each bioinspired model were printed and tested. They were pre-notched using a razor blade and jig to ensure consistently sized and perpendicular cracks 2.5 mm ± 0.09 mm in length. All samples were tested using the Instron 3367 load frame under ambient indoor conditions (approximately 22 °C and

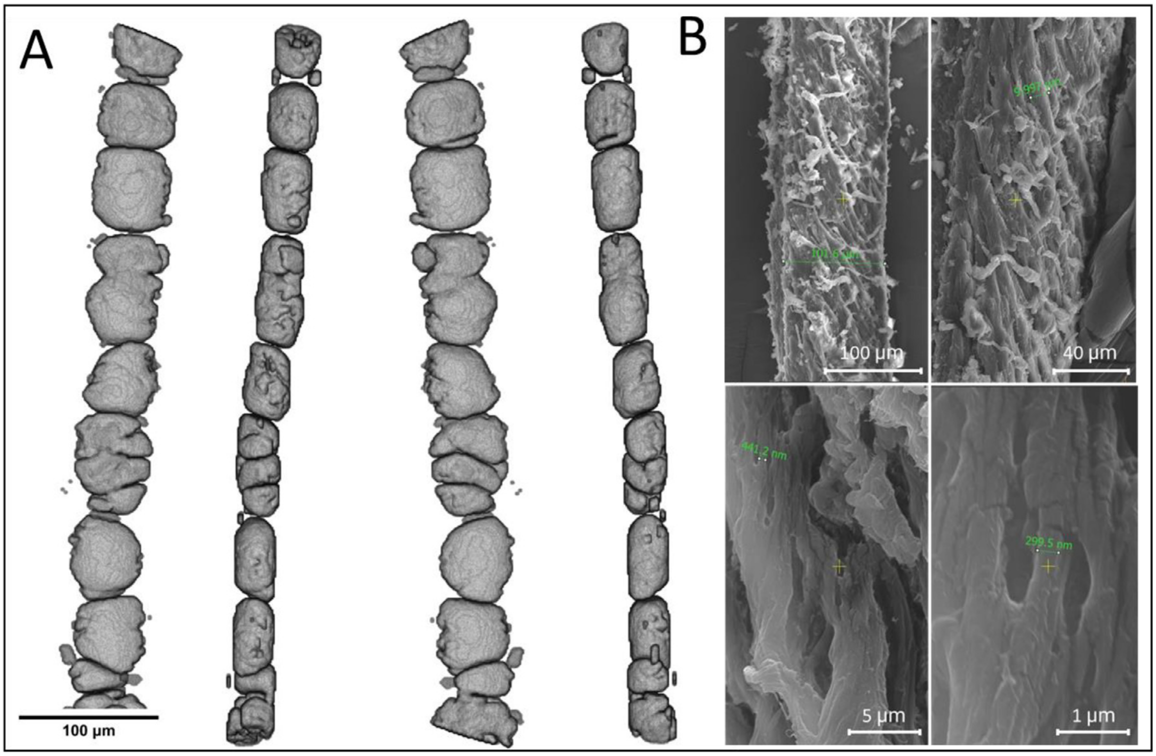

Fig. 2. A) Tubule structure extracted from microcomputed tomography scans of the horse hoof. B) Hierarchy of fibers in the horse hoof.

75% humidity). Samples were tested at 10 mm/min as per ASTM D5045 and the displacement and load until failure were recorded. Raw data were exported from the universal testing machine and normalized to consider the first 90% of the displacement in plotting load versus displacement curves on MATLAB. The energy absorbed for each model was calculated by measuring the average area under the curve for the model trials. Standard deviations for each model were also calculated and plotted.

Measurements of the sample dimensions were made before and after fracture using digital calipers. Videos of each experiment were recorded, and digital images of each sample post-fracture were taken. Videos were used to correlate the physical deformation behavior to the measured curves. Digital images were used to measure crack length using ImageJ (U. S. National Institutes of Health, Bethesda, Maryland, USA).

3. Results and discussion

3.1. Structure of the hoof wall

Tubular and fibrous arrangements reported by previous authors were confirmed by scanning electron microscopy (SEM) and microcomputed tomography (microCT). The gradients in tubule shape and density were consistent with previous observations of the hoof wall [3,4,9,11]. Fig. 2A shows an image of an extracted tubule from a microCT scan. The scans show that the hollow medullary cavities at the center of the tubules are not continuous structures but are segmented by bridges that span the empty space dividing the cavity into hollow pockets. These features have been noted before but never quantified [8]. Averaged measurements of bridge width, bridge density, cavity cross-sectional area, porosity of the central hoof wall cross-section, tubule density, and volume of an individual pocket are summarized in Table 1. Measurements of the tubule density agree with Reilly et al. [4] and Kasapi and Gosline [9], who found, respectively, 11-22 tubules/mm^2 and 10-25 tubules/mm^2 in the central region of the horse hoof wall. The average value for porosity (0.77% ± 0.3%) was lower than those measured by Huang et al. [8] (~3%). The measurements of the bridge width, bridge density, and average pocket volume are novel and have not been previously reported.

Table 1
MicroCT measurements of hoof features.

Bridge width (n=301^x)	10.3 ± 2.4 µm
Bridge density (n=16^y)	0.009 ± 0.002 bridges/µm
Pocket cross-sectional area (n=226^y)	365.8 ± 18.2 µm^2
Pocket volume (n=43^z)	40633.5 ± 12820.5 µm^3
Porosity (n=226^y)	0.77 ± 0.3%
Tubule density (n= 226^y)	15.91 ± 0.4 tubules/mm^2

x-Bridges, y-Tubules, z-Pockets.

SEM scans of fibers extracted during the cutting process show the hierarchy of fibers found in the hoof wall ranging from macrofibers on the scale of 100 micrometers down to embedded fibers that are just hundreds of nanometers in diameter. These features are shown in Fig. 2B.

3.2. Compressive response of the hoof wall

Keratin's mechanical properties are very hydration dependent, a phenomenon that has been reported in hooves [5,8,10] and numerous other keratinous systems such as horns, whale baleen [33], and hair [16,24,34–36]. Stress-strain curves for hoof samples compressed at five different strain rates for three different hydration conditions are shown in Figs. 3A-C. In Fig. 3A and B, the area between like samples is shaded in to establish a range of results and to better illustrate the trends observed under different testing conditions. A ductile-to-brittle transition was observed with the decrease in hydration as well as with increasing strain rate. Samples hydrated to 10% water content began to fracture around 0.1 strain and showed severe plastic damage after the compression tests. Due

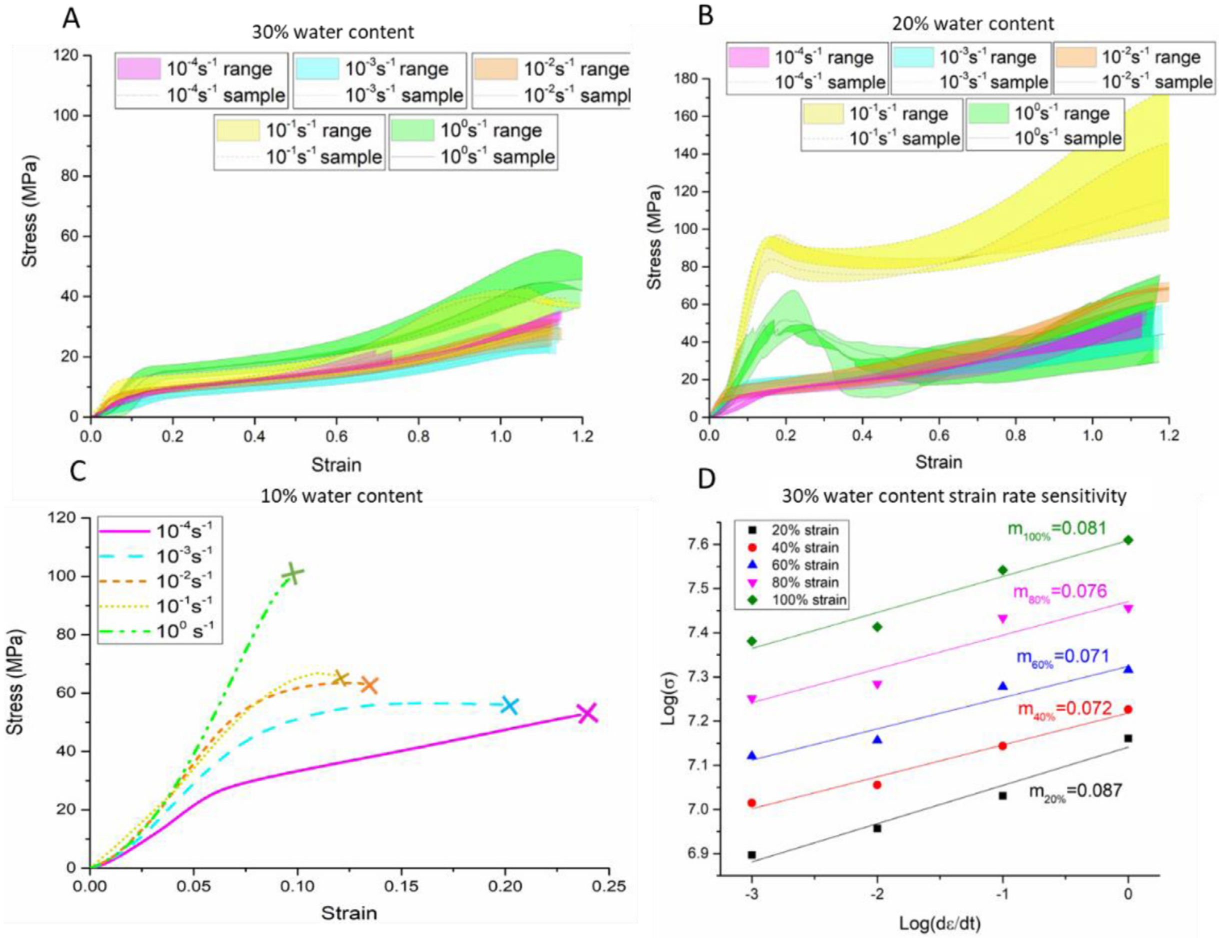

Fig. 3. Stress-strain curves of hoof samples compressed at five different strain rates (10^0 s^{-1}, 10^{-1} s^{-1},10^{-2} s^{-1}, 10^{-3} s^{-1} and 10^{-4} s^{-1}) for hydration states of A) 30%, B) 20%, and C) 10% water content by weight. For samples hydrated to 10% water content only the curve before the onset of fracture is shown. Due to cracks initiating at different strains for each sample at the lowest hydration state, a representative curve (the sample with the median ultimate stress) was selected to visualize the hoof wall behavior in the dry state.

to this brittle behavior, a wide variability in the curves was observed once the material began to crack. To visualize the data more clearly, only the portion of the curve before cracking begins is plotted in Fig. 3C. Since samples failed at different strains, plots showing the range of sample curves do not effectively convey the behavior of the drier hoof wall. Instead, the sample with the median ultimate stress for each strain rate was chosen to serve as a representative curve. In the 10% water content condition, brittle fracture dominates; it is determined by discrete microplastic buckling and fracture events. Generally, samples tested at higher strain rates fractured at lower strains and at higher stress levels as suggested by Fig. 3C, however more samples would need to be tested to make this a statistically valid assertion. For each strain rate there was a wide range of ultimate stress and strain values. For these drier samples, catastrophic events dictate the material response.

For the most hydrated samples (30% water content) there is a noticeable and consistent strain rate effect. A linear shift in stress levels at specific strains can be seen with increasing strain rate. Samples tested at 10^{-4} s^{-1} fit this trend well initially but then diverge at higher strains, likely due to drying effects during testing. As such, the reported stress levels for this strain rate are likely inflated due to inconsistent hydration conditions during testing.

At 20% water content by weight, samples tested at the highest strain rate continue to show a brittle behavior. This response is visualized by the green shaded region in Fig. 3B where there is a long elastic regime, reaching a high stress of 50-65 MPa, followed by a precipitous drop in stress, signifying plastic damage and fracture. When loaded at 10^{-1} s^{-1}, the samples exhibited a similar initial behavior as the samples loaded at 10^0 s^{-1}. However, they did not fail in a brittle manner between 0.1 and 0.2 strain and were able to exceed the maximum stress of samples tested at the faster strain rate. On the other hand, samples tested at 10^{-2} s^{-1}, 10^{-3} s^{-1}, and 10^{-4} s^{-1} express elastomer-like behavior. Thus, the ductile-to-brittle transition is captured at 20% water content by weight. Such a ductile-to-brittle transition with increasing strain rate is consistent with previous observations for toucan rhampotheca [37] and pangolin scales [20].

As mentioned above, all of the samples hydrated to 30% water content by weight display ductile behavior and are significantly softer than those in the other two hydration conditions. The stress-strain curves at 10^0 s^{-1} and 10^{-1} s^{-1} are shifted upward relative to the other strain rates. Only a marginal difference between 10^{-2} s^{-1} and 10^{-3} s^{-1} is observed for this hydration condition, but the curves for the latter strain rate tend to be comparatively shifted down. As previously mentioned, samples tested at 10^{-4} s^{-1} have higher stress values than expected, likely due to drying during testing. Samples hydrated to 30% water content also showed very little visible damage and even exhibited noticeable shape recovery after the load was released. This shape recovery has been previously observed in feather [38] and horn [16] keratin. The strain rate sensitivity, defined as $m = \partial \ln\sigma / \partial \ln\dot{\varepsilon}$ is displayed in Fig. 3D

Table 2
Elastic modulus values for hoof samples tested at different hydrations and strain rates.

Strain rate	10% ± 1% water content	20% ± 2% water content	30% ± 2% water content
10^{-4} s^{-1}	547.4 ± 251.9 MPa	105.1 ± 22.5 MPa	48.4 ± 26.4 MPa
10^{-3} s^{-1}	600.0 ± 99.1 MPa	281.5 ± 40.1 MPa	56.6 ± 25.8 MPa
10^{-2} s^{-1}	774.9 ± 188.4 MPa	439.3 ± 90.3 MPa	169.2 ± 51.1 MPa
$10^{-1}s^{-1}$	743.4 ± 151.1 MPa	512.8 ± 120.5 MPa	105.1 ± 35.1 MPa
10^{0} s^{-1}	1218.9 ± 171.5 MPa	941.9 ± 120.7 MPa	164.6 ± 17.3 MPa

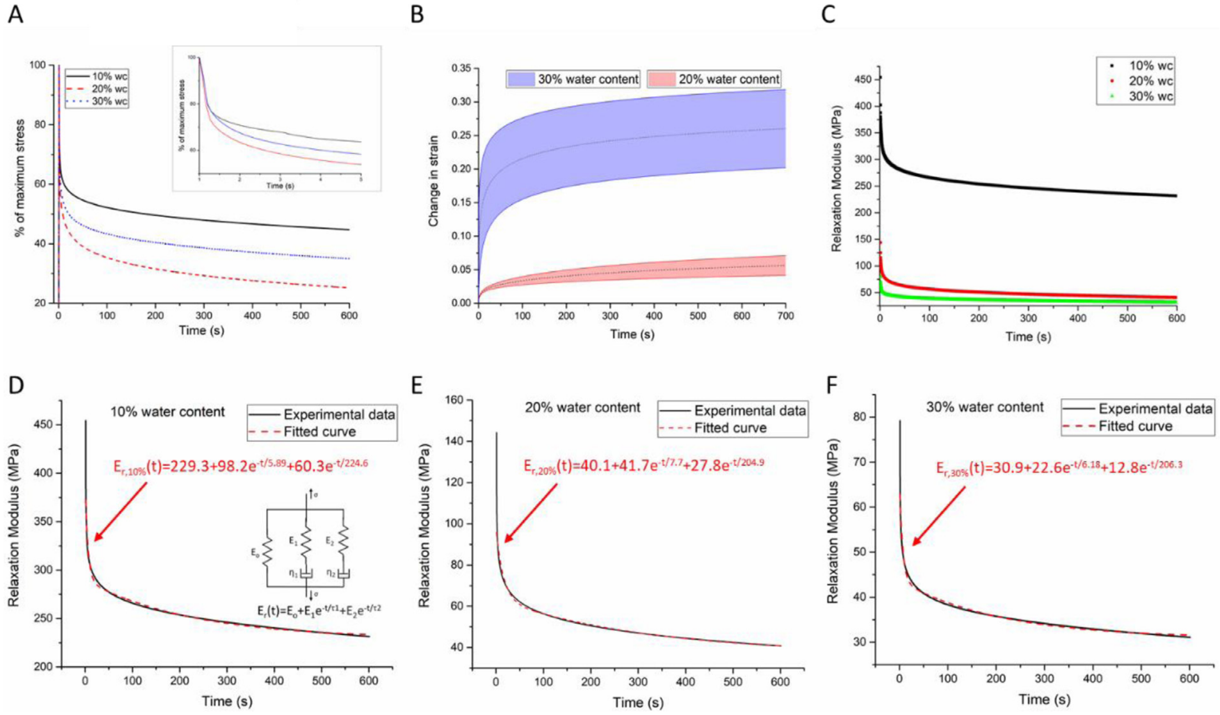

Fig. 4. When compressed, the hoof wall displays viscoelastic behavior that varies with hydration. A) Normalized relaxation data vs time. Inset shows initial relaxation period. B) Creep test of hoof samples hydrated to 20% and 30%. C) Relaxation modulus for each hydration state as a function of time. Fitted curves of three-term Prony series compared with experimental data for D) 10% (and Simplified Maxwell-Weichert model with generalized equation used to model viscoelastic behavior of the hoof wall) E) 20%, and F.) 30% water content by weight.

and ranges from 0.072 to 0.087. These values are in line with other keratins: baleen (0.09 to 0.11) [33], pangolin scales (0.06) [20], and hair (0.06) [39]. These biopolymers have a response similar to synthetic polymers, such as Poly(methyl methacrylate) (PMMA) (0.07) [33].

The elastic modulus decreases with increasing hydration and generally increases with increasing strain rate, in agreement with previous work [5,10]. Table 2 shows the measured elastic modulus for each condition. The linear elastic regime, seen in Fig. 3A-C, shrinks with increasing hydration. The water molecules in the hydrated hoof act as a plasticizer. The hydrogen bonds that stabilize the α-helix structure of the keratin molecules and weakly crosslink adjacent polymer chains are interrupted, reducing the stiffness of the material dramatically [40]. At low hydrations, the keratinous hoof wall behaves like a hard plastic, exhibiting plastic deformation at relatively low strain. This behavior results in a stress plateau beginning at ~0.15 strain as the damaged material is less capable of resisting stress once fractures have been introduced. At higher hydrations, the material behaves more like an elastomer. It exhibits a short initial elastic regime before a slow, steady increase in stress up to approximately 45% strain. At this point, most of the pores have collapsed, and the densified material sees a steep increase in stress with increasing strain. However, very few fractures are observed, and the onset of plastic deformation is significantly delayed.

Fig. 4A shows the averaged curves (N=5) of stress relaxation tests over a range of 600 s. To better compare samples, the percentage of maximum stress was plotted versus time. Interestingly, the middle hydration level of 20% water content by weight exhibits the most relaxation relative to its initial stress level, losing nearly 75% of its maximum stress over a 10 min relaxation period. Meanwhile, the 30% water content by weight samples approached a 65% decrease in stress, while stress in the 10% water content by weight samples only dropped by about 55%. It stands to reason that the dry samples would exhibit less viscoelastic relaxation, but the results of the 30% water content by weight samples seem anomalous. This is likely due to the higher absolute stress level present in the 20% water content samples when they are compressed to the same strain, since the 20% water content samples have elastic modulus values ~2-5 times higher than those of the 30% water content samples. This notion was confirmed by creep tests on the two sets of samples hydrated to 20% and 30% water content, where the samples are loaded to the same stress level and then the change in strain over time is measured. The results of these tests are displayed in Fig. 4B and suggest that samples hydrated to 30% water content are significantly more viscoelastic, with an average change in strain of 26.02 ± 5.83% after 700 s compared to that of the 20% water content samples which had an average change in strain of just 5.62 ± 1.48% over the same time period.

Water, by infiltrating in the structure, disrupts hydrogen bonds that stabilize the keratin structure, allowing the keratin fibers to slide past each other and rearrange more easily. This behavior has interesting implications for the naturally occurring hydration gradient in the hoof wall. Kasapi and Gosline [9], Bertram and Gosline [6], and Douglas et al. [10] discuss how this gradient leads to a decrease in strain differential between the stiff hoof wall and the soft interior tissue; however, the authors do not explore or discuss the viscoelastic implications of this hydration gradient. Unfortunately, there is no clear consensus for the natural hydration condition of the horse hoof *in-vivo*. For example, Leach [5] reported an average of 20.0% water content at the outer wall and 27.6% at the inner wall, while Douglas et al. [10] reported a moisture content of 27.9% at the outer wall and 35.5% at the inner wall. In either case, it seems that the stiffer exterior portion of the hoof wall may have an optimal water content for increased stiffness while maximizing the viscoelastic nature of keratin that improves its energy dissipation and durability. Furthermore, even with the gradual gradient identified by previous studies, one would expect the hydration difference and therefore stiffness difference through the thickness of the hoof to give rise to internal shear stresses as the hoof is loaded. However, the more rapid viscoelastic recovery of the hoof when hydrated to 20% water content likely helps overcome this issue. For instance, when compressed to 10% strain, hoof samples hydrated to 20% water content experience an average stress 1.77 times that of samples hydrated to 30% water content. However, this ratio drops to 1.67 after 1.5 s and then 1.57 after 22 s. After 600 s this ratio is reduced to just 1.31. Meanwhile, samples hydrated to 10% water content experience an initial stress 5.67 times larger than that of the 30% water content samples. After 1.5 s, 22 s, and 600 s this *grows* to 6.11, 6.61, and 7.44, respectively. An exterior hydration of ~20% water content allows the hoof to harness the benefits of a stiff exterior while also minimizing internal shear stress via rapid viscoelastic relaxation. Of course, these tests only account for variations in hydration, but not any of the structural differences that occur through the hoof wall thickness, which may further improve this optimization.

A closer look at the initial phase of relaxation can be seen in the inset of Fig. 4A. Immediately after the stress relaxation begins, the samples experience a linear drop in stress before entering a region of gradual decay. The samples hydrated to 20% water content experience the steepest drop in stress in this linear region, followed by the 30% water content samples and finally the 10% water content samples. Several of the relaxation curves for the 10% water content samples lack the smoothness seen in the other two sets of curves. In these samples, a sudden change in the relaxation rate can be observed between 3 and 4 s, and this is reflected to a lesser degree in the averaged curve. This behavior is likely the result of shifting plastic deformation that occurred during loading.

The viscoelastic behavior of keratinous materials has previously [39] been quantified using a simplified version of the Maxwell-Weichert model (Fig. 4D) which uses two Maxwell elements (a spring and dashpot in series) and a spring in parallel. The relaxation modulus of the system can be represented by the following three-term Prony series:

$$E_r(t) = E_o + E_1 e^{-t/\tau 1} + E_2 e^{-t/\tau 2}$$

where t is the time elapsed since the beginning of the relaxation period, E_1 and E_2 are the elastic moduli of the springs in the Maxwell elements, E_o is the elastic modulus of the remaining spring, and τ_1 and τ_2 are characteristic relaxation constants defined as the ratio between the viscosity, $\boldsymbol{\eta}$, of the dashpot and the elastic modulus, E, of the spring in each Maxwell element. The two-step relaxation process observed in keratin has been attributed to two distinct mechanisms at different hierarchical levels. The shorter relaxation time, measured to be between 11 s and 14 s in hair [39], is the result of relaxation of the larger scale features such as cells, lamellae, and tubules while the longer relaxation time, determined to be about 207 s in human hair, is thought to be the result of nanoscale features, like the IFs. Fig. 4C shows plots of the relaxation modulus for each hydration condition. These curves were then fitted to the generalized Maxwell-Weichert equation. The calculated curves are plotted alongside the experimental data in Figs. 4D-F. The resulting equations are:

$$E_{r,10\%}(t) = 229.3 + 98.2e^{-t/5.89} + 60.3e^{-t/224.6}$$

$$E_{r,20\%}(t) = 40.1 + 41.7e^{-t/7.7} + 27.8e^{-t/204.9}$$

$$E_{r,30\%}(t) = 30.9 + 22.6e^{-t/6.18} + 12.8e^{-t/206.3}$$

The hoof wall samples hydrated to 20% had the largest short-term relaxation constant and the smallest long-term relaxation constant. Studies on hagfish slime threads suggest that the amorphous matrix in which the IFs are embedded is likely the most susceptible to hydration sensitivity [24,41]. In this context, it makes sense that the more hydrated samples would have a noticeably lower long-term relaxation constant which is associated with nanoscale structures. Meanwhile the driest samples, hydrated to 10% water content, exhibit the fastest short-term relaxation time due to plastic relaxation of minor cracking and delamination that occurred during loading.

Human hair has characteristic relaxation times of ~207 s and ~11 s [39]. The larger relaxation time is remarkably consistent with the results of this study (224.6 s, 204.9 s, and 206.3 s). The results agree well with the assumption that this relaxation time represents keratin's nanoscale features which should be similar in both systems [8,36]. The shorter relaxation time, however, is significantly different. This finding also makes sense, considering that the hoof has significantly different mesoscale features than hair. With a lower short-term relaxation time (5.89-7.7 s), the tubule reinforcement/intertubular lamellae in the hoof seem to relax quicker than the cortical structure of hair (11 s). Furthermore, in the hoof, the Maxwell-element moduli for the large-scale features, E_1, are 1.5-1.75 times larger than the moduli of the smaller features, E_2, whereas in hair, this is reversed, with E_2 being 1.5-1.75 times larger than E_1 [39]. This finding indicates that the hoof has a steeper initial decay of stress and that the short-term relaxation that arises from the hoof's mesostructure is more dominant than in other keratinous materials. For example, after 3 s, the E_r for hair drops to 95.9% of its initial value while that of hooves drops to 89.7%, 87.4%, and 86.6% for 10%, 20%, and 30% water content, respectively. After 10 s these values become 89.5% (hair), 78.6%, 71.1%, and 71.7% (hoof). With just a matter of s between each footfall for a galloping horse [42,43], being able to dissipate compressive stress via viscoelastic relaxation more quickly is advantageous for preventing the build-up of stress during the repeated loads of locomotion. These tests suggest that hooves can improve this capability over other keratinous materials with their mesostructural features, highlighting yet another benefit of the hoof's unique configuration.

3.3. Impact performance of hoof wall

Similar to the quasistatic compression experiments, there was a dramatic effect of the degree of hydration on the impact response. Fig. 5A shows sample dimensions and extraction location from the hoof wall. Samples hydrated at 50% RH (Relative Humidity) showed almost no damage regardless of impact energy. Many of these samples simply bent under impact, rather than fracturing or cracking. These samples were so ductile that they were able to bend in half and squeeze into the lower aperture upon impact. They could be

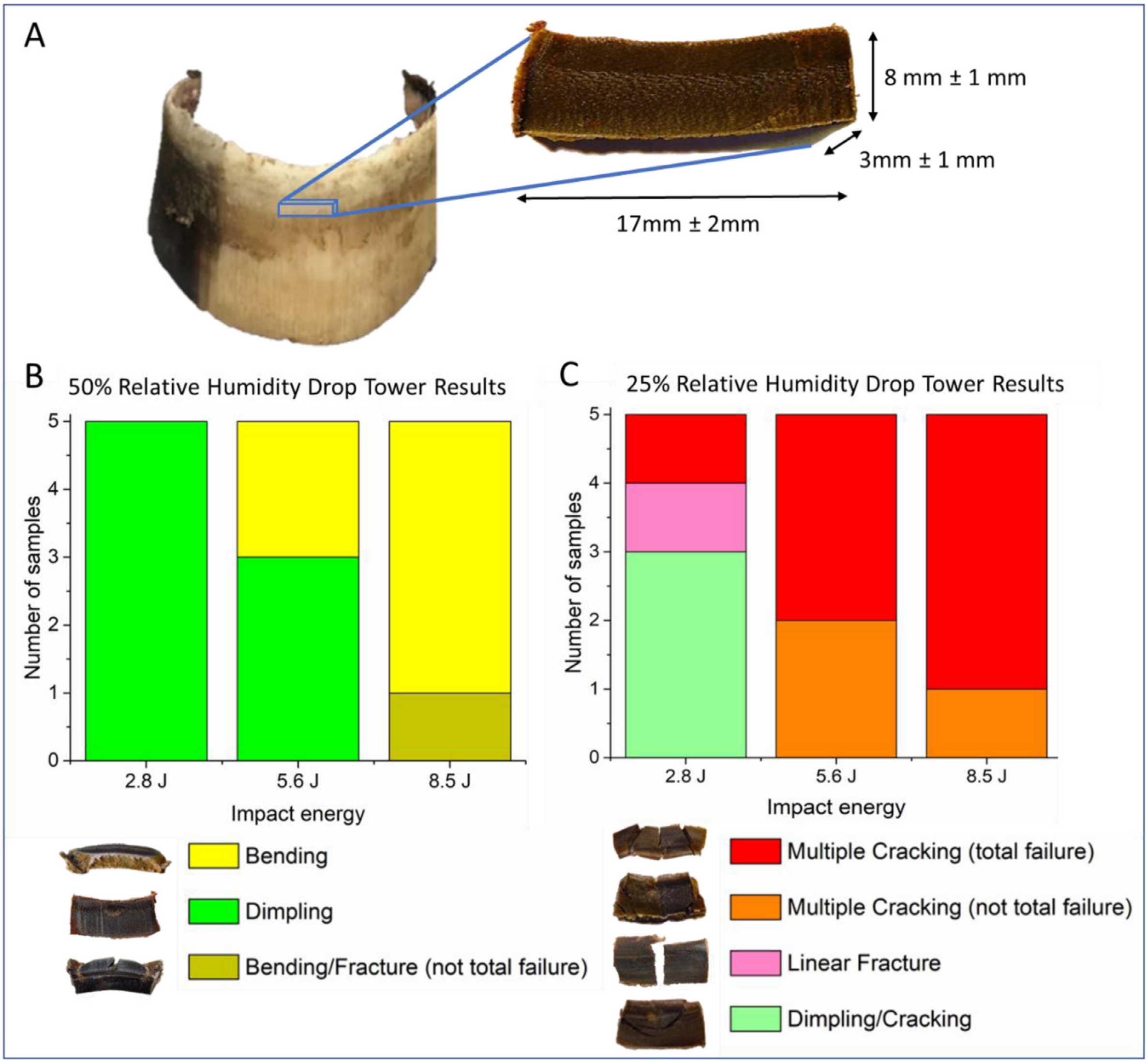

Fig. 5. Drop tower experiments were performed on hoof wall samples. A) Sample dimensions and location of extraction. Failure mechanism histograms for different impact energies for samples equilibrated at B) 50% RH (Relative Humidity) and C) 25% RH.

removed and straightened to their initial shape with minimal noticeable damage. Only one sample impacted at the highest energy exhibited cracking after being bent to nearly 180°. The samples hydrated at 25% RH, however, showed significant damage regardless of impact energy. This is indicative of a ductile-brittle transition between 25% RH and 50% RH for the hoof wall. The severity of damage in the samples also increased with increasing impact energy. Figs. 5B and C indicate the damage observed in the samples after drop tower testing at different impact energies for 25% RH and 50% RH, respectively.

The fracture morphology depends, by virtue of the anisotropy of the structure, on the orientation of the propagation path. For the drop tower fractured specimens, the state of stress is complex and not controlled, and so is the fracture path. Nevertheless, it was possible to identify some important characteristics. Fig. 6A shows two principal fracture planes: parallel and perpendicular to the orientation of the tubules in agreement with previous studies [6,7,9,12]. When the crack front is perpendicular to the tubules, it forms steps aligned with weak planes in the intertubular matrix. For the other extreme case, where the crack plane is aligned with the tubules, the crack front tends to meander between the tubules, since the peritubular material has a higher strength than the matrix (Fig. 6B). These different modes of fracture corresponded to varying impact energy with fractures tending to form perpendicular to tubules at higher impact energies and along the tubule axis at lower ones. Kasapi and Gosline [12] do not mention these phenomena during their fractography analysis of compact tension tests at different strain rates, instead only making note of differences due to location in the hoof wall. At the next spatial scale, (Fig. 6C-E) there is also a distinct effect of strain rate. At low impact energies cracks develop between tubular and intertubular fibers. When the material fails these cracks eventually propagate longitudinally along the tubule as shown in Fig. 6A. At intermediate impact energies, crack initiation phenomena similar to the low impact energy samples were observed; however, longitudinal tubule pull-out could also be seen. At high impact energies, individual tubules were shorn laterally from the matrix while cracks traveled in a stepwise pattern through the intertubular material. Finally, on the microscale and below, failure of the horse hoof involves rupturing the hierarchy of fibers shown in Fig. 2B.

Figs. 7-9 provide observations that elucidate the mechanisms of fracture propagation and toughening at the meso and microscale. SEM images of the post-impact crack interfaces of the 25% RH samples reveal that the failure mechanisms depend on impact en-

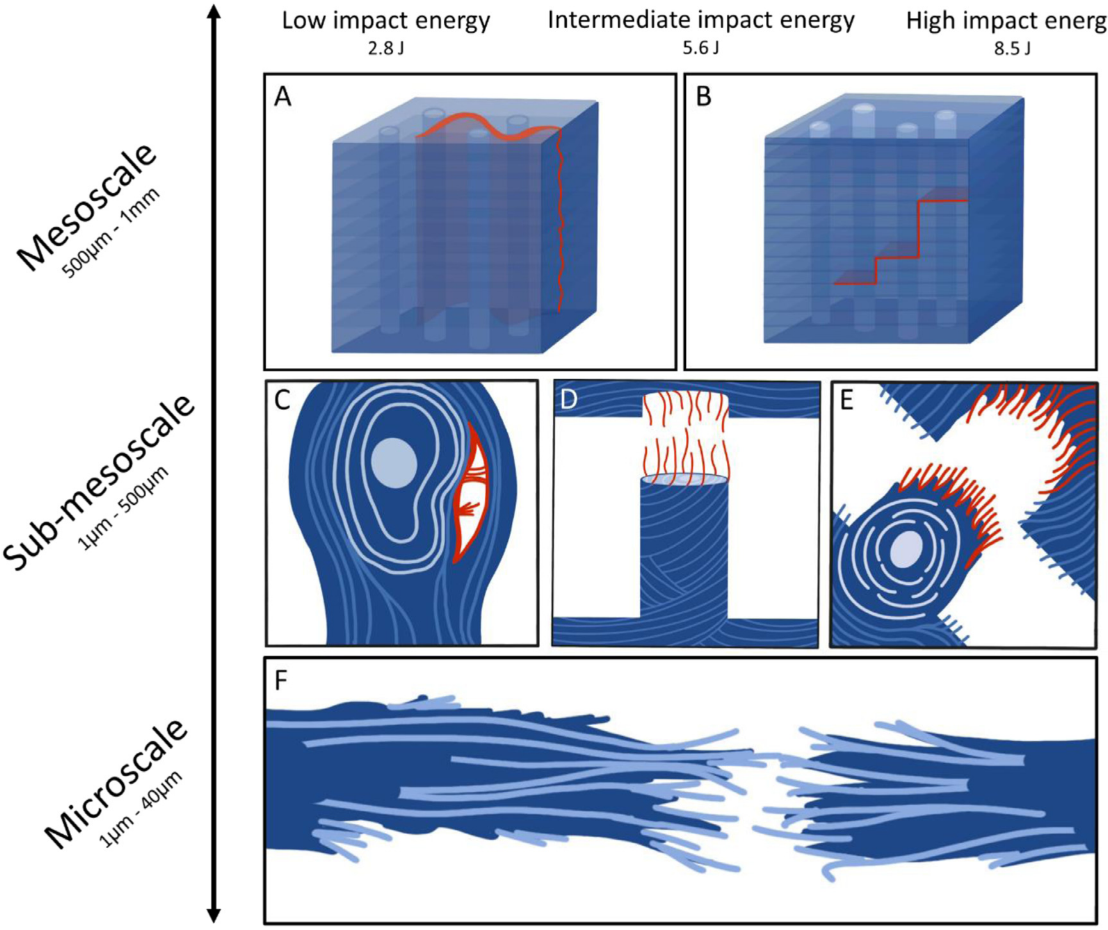

Fig. 6. Schematic showing the failure mechanism of each length scale's characteristic structures at different impact energies. The microscale depicts the ubiquitous fiber rupture, the sub-mesoscale shows tubule splitting/cracking, tubule pullout, and tubule tearaway, while the mesoscale depicts crack deflections at the tubular (low and intermediate impact energies) and lamellar (high impact energies) interfaces. Red lines indicate points of failure such as fiber rupture or cracking, light blue lines indicate tubular fiber orientation, and dark blue lines correspond to fiber orientation in the intertubular matrix. Fig. by Brooke Stephenson.

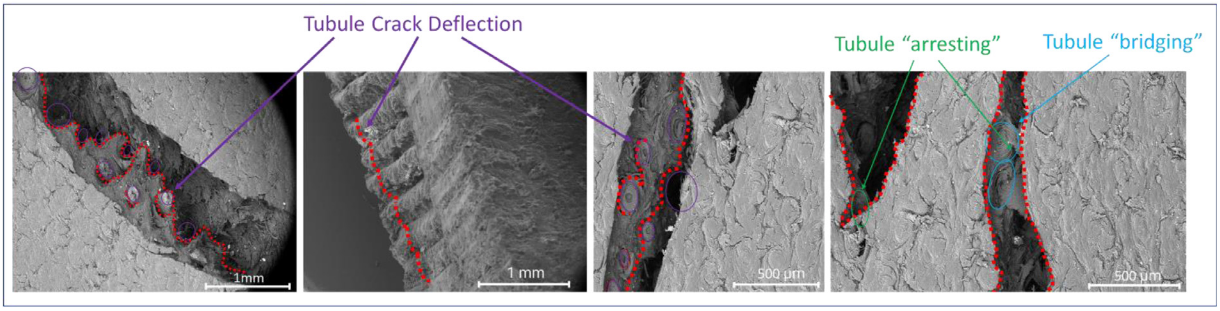

Fig. 7. At the lowest impact energies the tubules cause significant crack deflections resulting in tortuous fracture surfaces. Tubules were also noted for the first time to bridge cracks, providing an extrinsic toughening mechanism, and arresting crack interfaces in their fibrous cortical layers.

ergy and highlight some of the features that make the hoof so energy absorbent under impact. At the lowest impact energy of ~2.8 J, cracks formed in several samples. SEM images of these crack interfaces show that significant deflection occurred along the tubule/matrix interface (Fig. 7). These deflections cause the crack to take a meandering, energy-absorbent path. This result is similar to that of Mirkhalaf et al. [44] who determined that introducing planes of weakness into a brittle material can be used to create tortuous crack paths and improve toughness. Small cracks were also observed around some of the tubules which suggest the onset of delamination between the tubule cortical layers and the surrounding matrix. Several other fracture mechanisms centered around the tubules were observed, including tubules arresting cracks and bridging cracks, as shown in the right-most image in Fig. 7. In the instance of tubule arresting, cracks were halted when their tip reached a tubule interface. Meanwhile, in the case of tubule bridging, cracks passed through the tubules, but the two surfaces of the crack were held together by the intact tubule structure. This extrinsic toughening mechanism has been observed with perpendicular fibers spanning cracks in biological systems such as bone [45], but not as a result of tubules running parallel to the crack interfaces. Horse hooves are unique since they have high-aspect ratio reinforcing elements (tubules) that are physically intertwined with the surrounding fibrous matrix. This feature will

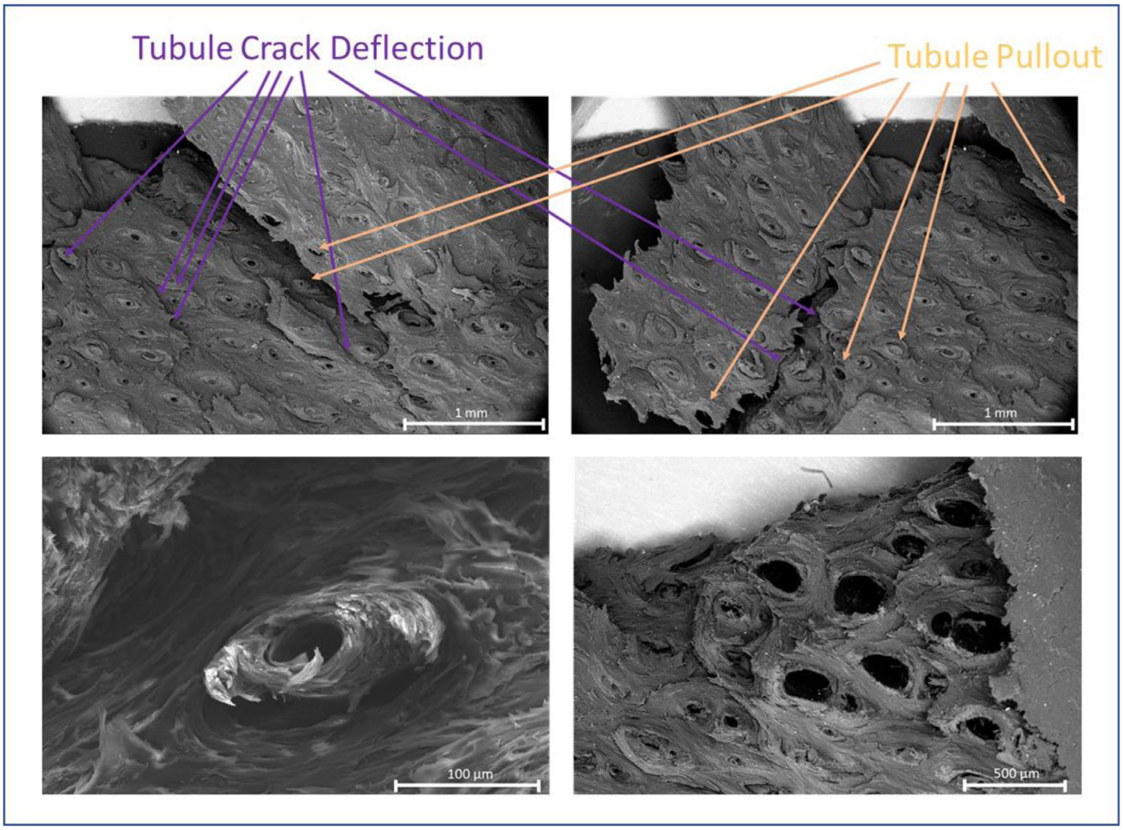

Fig. 8. At the intermediate impact energy tubules cause crack deflections and pull out of the matrix. The top two panels show SEM images containing multiple examples of these phenomena. The bottom two panels show a tubule that has debonded from the matrix in the longitudinal direction (left), as well as the remnant matrix.

be discussed in greater depth later in this section but is important for understanding how tubules are able to span fracture surfaces and arrest crack growth.

At the intermediate impact energy of ∼5.6 J, tubules not only cause crack deflections but also begin to delaminate entirely from the surrounding matrix. This mechanism is similar to the fiber pullout observed in synthetic composites [46–49] and has been noted in other composite biological materials like wood and bone [50,51]. As the hoof wall flexes under impact, significant stress concentrations build up at the interface between the reinforced tubules and the softer matrix. These magnified stresses cause the tubules to debond and slip out of the matrix. Several examples of this behavior are noted in the top images of Fig. 8. An example of a pulled-out tubule can be seen in the bottom left pane of Fig. 8 while the remnant matrix is shown in the bottom right.

Another important implication of the hoof wall's tubular reinforcement is the way in which the tubules adhere to the surrounding matrix. Unlike most synthetic fiber reinforced composites, which grip the matrix with friction, the tubular reinforcement in the hoof is physically attached to the matrix with intertwined fibers that span the tubule/matrix interface. Therefore, to induce tubule pullout or tubule tear-away the bonds that hold these fibers together need to be overcome. Torn fibers between the matrix and tubule after impact can be seen in Figs. 9A-C. Figs. 9D-F show the hierarchy of torn fibers on the surface of a tubule that has ruptured from the surrounding matrix with each successive image revealing a finer embedded fibrous structure. We hypothesize that this physical attachment can increase the value for κ, the bond modulus of the reinforcement, as well as increasing the amount of energy that is dissipated when tubules rupture from the surrounding matrix. In synthetic composites, the degree of bonding across the interphase region (the interface between fiber and matrix) is vital and can govern the mechanical potential of fiber reinforced composites [52,53]. Significant research has gone into improving the adherence of fibers to the matrix including the use of fiber surface modifications via dip coating [54], functionalized nanoclay grafting [55,56], nanofiber chemical vapor deposition [57,58], and chemical sizing agents [59–61]. The hoof's bottom up self-assembly allows it to create fiber reinforcement that is physically attached to the surrounding matrix with a hierarchy of fibers. This structural motif can serve as inspiration for future designs of fiber reinforced composites.

The critical force, P_{crit}, required to induce fiber pullout in engineered composites is often based on the assumption that the bonding between the reinforcement and surrounding matrix is purely frictional. In the case of the hoof, where additional force is required to fracture the fibers that traverse the interphase boundary of the reinforcement, an additional term can be added:

$$P_{tubule} = \sigma_{fibers} * A_{fibers} * \rho_{fibers} * 2\pi r l$$

where σ_{fibers} is the tensile strength of the keratin fibers, A_{fibers} is the average cross-sectional area of the fibers, ρ_{fibers} is the density of fibers per unit area, r is the radius of the tubule, and l is the length of the tubule. However, as previously noted, many of the tubules in the hoof are elliptical rather than circular in cross-section, which increases the surface area of the tubules and therefore the number of fibers that can span the interphase region.

At the highest impact energy of ∼8.5 J, the intertubular lamellae begin to play a more dominant role in the fracture path of the hoof wall. Figs. 9G-I shows several of these fracture surfaces. This failure pattern increases the surface area of fractures in the sample as cracks move horizontally through the sample rather than traveling down along the tubule axis. At the highest impact energy, the tubule-matrix interaction also begins to change. Rather than

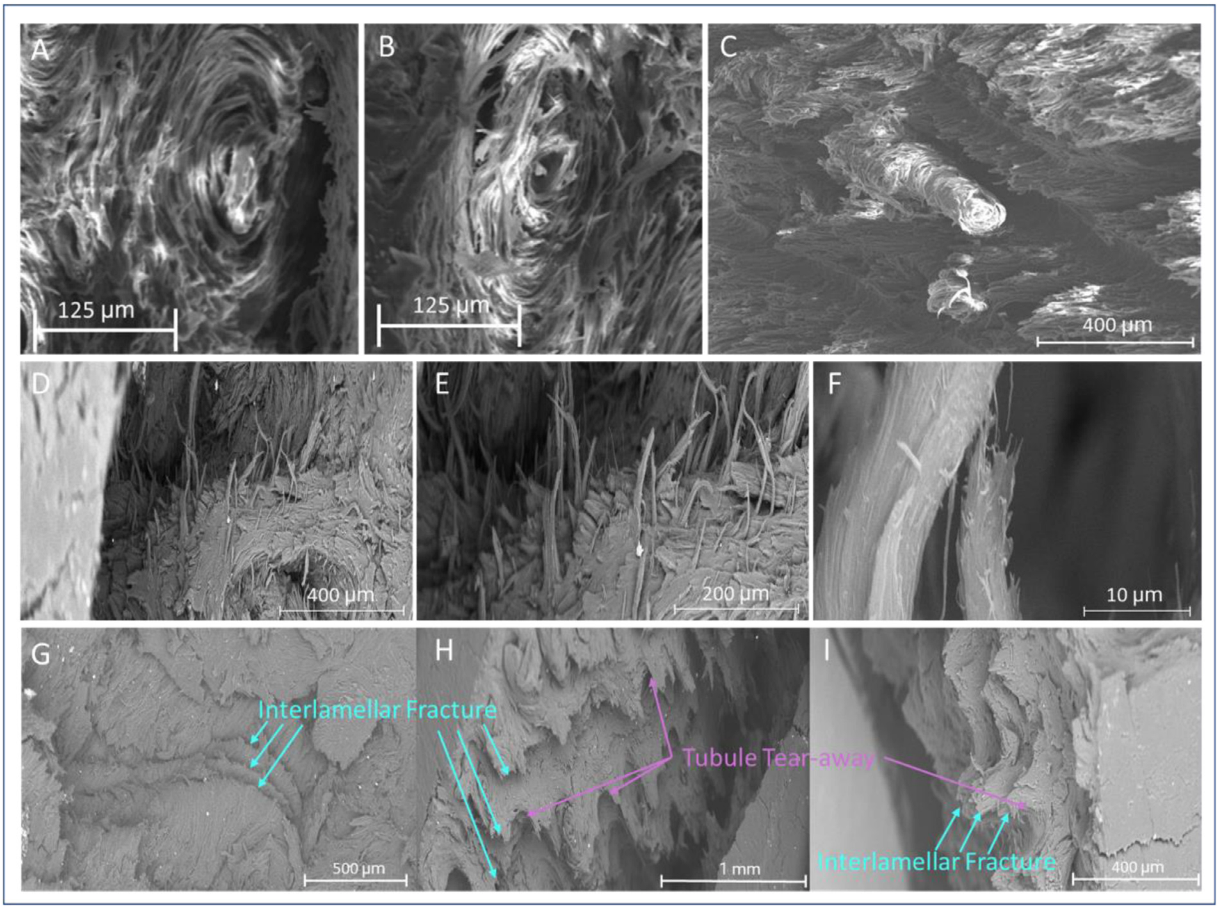

Fig. 9. Unlike engineered composites, the hoof wall's reinforcing elements are physically attached to the surrounding matrix. A-C) SEM images of post-impact specimens showing torn fibers that once connected the reinforced tubules to the matrix. D-F) SEM images of the same ruptured tubule showing the hierarchy of fibers involved in the interphase connection. G-I) At the highest impact energies, the intertubular lamellae dominate the fracture path as cracks propagate along the boundaries between the layers. At these impact energies, tubules rupture from the matrix laterally rather than longitudinally.

pulling tubules out of the matrix in the longitudinal direction, the impact causes tubules to tear away from the matrix in the transverse direction.

These findings generally agree with higher strain rate compact tension tests performed by Kasapi and Gosline [12]. However, they differ in that samples impacted at higher energies do not have more smooth fracture surfaces. These results also differ significantly from quasi-static tests [7,9] on the hoof wall which showed that the intertubular material nearly always dominates the fracture path. One feature that was noted by Kasapi and Gosline [9] is the variation in IF alignment through the hoof. Under quasi-static loading, this IF arrangement led to crack deviations away from the living tissue at the interior of the hoof. A similar phenomenon was observed after drop tower impacts but to a much lesser extent. In nearly all fractured samples, cracks traveling toward the interior exhibited a sharp bend at the same location. Several examples of this deflection can be seen in the images on the left half of Fig. 10. SEM images, shown on the right of Fig. 10, revealed that this deflection occurred in the region where there was a change in fiber alignment. Since the IFs are aligned within the macrofibers, the change in macrofiber orientation corresponds well to the crack deflection mechanisms found by previous studies. However, likely due to the higher impact energies of the drop tower tests, this change in orientation was not enough to fully deflect the crack away from the interior, but only to cause a minor deviation in the crack path. Regardless, this suggests that macroscale fracture control properties of the hoof arise from its fibrous composition. Another cause of this deflection could be the change in tubule shape and density in this region that was reported by Kasapi and Gosline [9], Reilly et al. [4], and Leach [5]. Here, there is a transition from smaller partially elliptical tubules to large circular ones which may lead to the change in crack path.

Huang et al. [8] observed fibrous bridges spanning the hollow medullary cavities of the tubules and hypothesized that these increased stability of the tubule. Indeed, these bridges do seem to play a structural role in the hoof as many were found fractured after impact while the rest of the tubule was left mostly intact. Several SEM images of this phenomenon can be observed in Fig. 11.

3.4. Bioinspired designs

These designs were generated to test the hypotheses developed as a result of the observations of the fracture retardation mechanisms made in the drop tower tests. Several simulated mesostructures created by additive manufacturing were tested in the drop tower setup and subsequently in a more controlled geometry in which a crack was generated with well controlled orientation (quasistatic fracture toughness tests).

3.4.1. Dynamic tests (drop tower)

Computer aided design depictions of each model is shown in Fig. 12A. Model 1 serves as a control sample with no features and consisting only of matrix material. Model 2 incorporates uniformly distributed hollow cylindrical cavities, representing the medullary

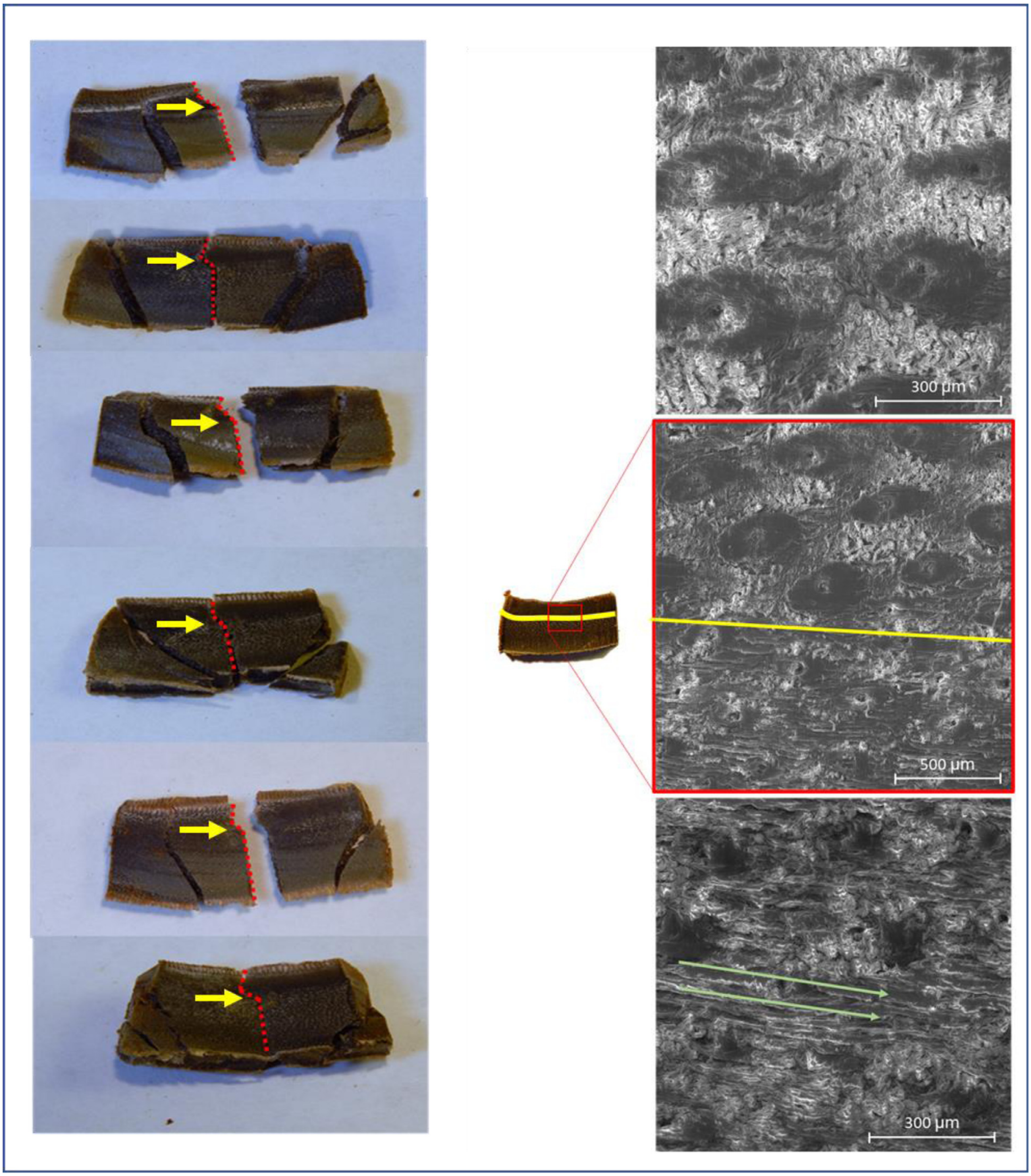

Fig. 10. Fiber orientation within the hoof leads to crack deflections during fracture. (Left) images of samples after drop tower testing showing crack deviation near the interior of the hoof wall. Crack path is highlighted by the dotted red line. The deflection is emphasized by the yellow arrow. (Right) SEM images taken around the deflection zone showing a change in the orientation of the fibers. In the top image, taken above the yellow line, fibers are oriented perpendicular to the cross-section. In the bottom image, taken below the yellow line, fibers run parallel to the cross section, as shown by the green arrows. The middle image shows the transition region where the orientation of the fibers changes.

cavities found in the hoof wall. Model 3 incorporates the tubular density gradient found in the hoof wall, with the hollow cylinders more congested towards the 'exterior' end of the sample and fewer near the 'interior'. Model 4 maintains the same uniform tubular arrangement as Model 2 but incorporates reinforcement material around each cavity. Model 5 maintains the same uniform distribution but adopts the shape gradient feature as outlined in Kasapi et al. [9], which shows that tubules in certain regions are more elliptical than in other portions of the hoof. Model 6 incorporates the shape gradient as well as the density gradient and has a tubular structure most similar to the actual hoof. The final two models were designed to test the intertubular lamellar features by emulating a 3:1 matrix to soft layer ratio. Model 7 incorporates the soft layers into a featureless matrix with no tubules. Model 8 has the same realistic tubule arrangement as Model 6 but adds soft lamellae into the intertubular matrix. Care was taken to ensure that each multi-material model consisted of the same volume fraction of tubular reinforcement in spite of the design differences.

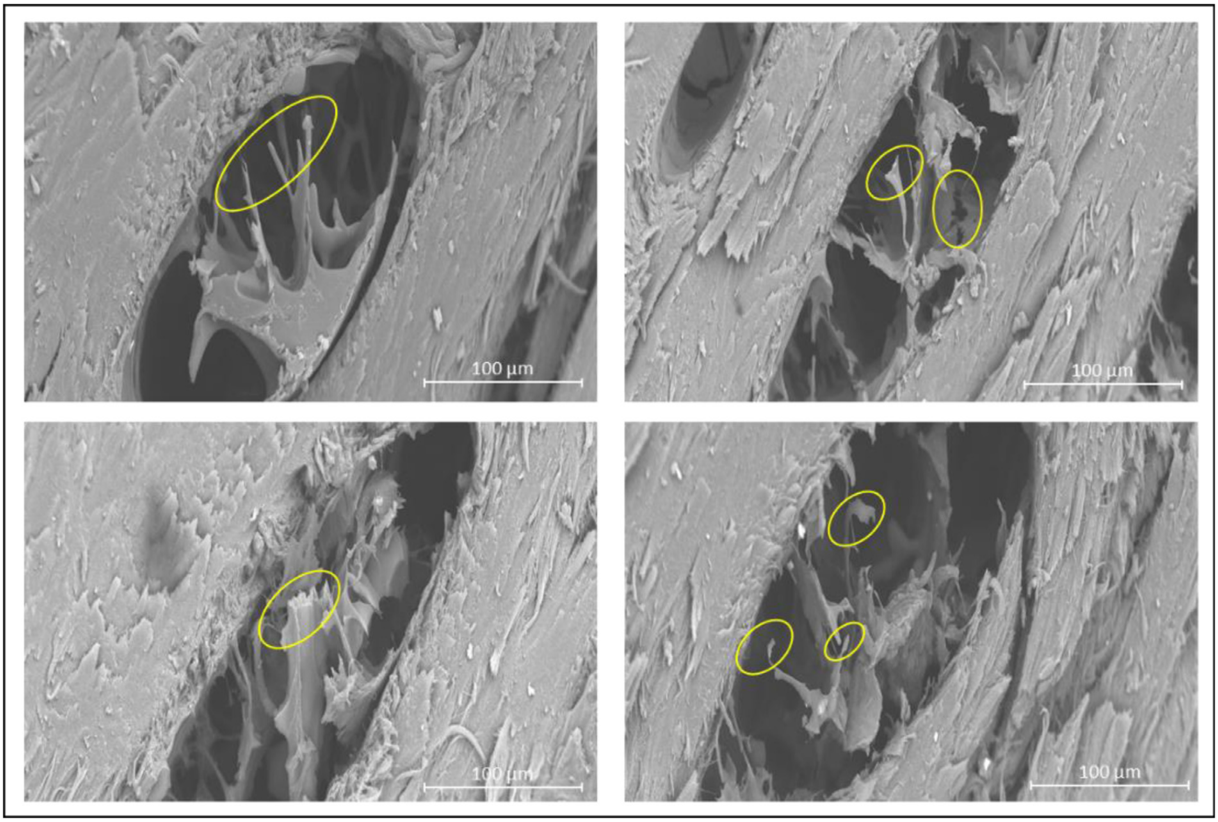

Fig. 11. SEM images of fractured tubule bridges. These structures fractured prior to the rest of the hoof wall suggesting they play an important role in the structural stability of the hoof wall.

The introduction of tubules into single phase samples led to an appreciable increase in damage volume between the featureless Model 1 and the uniformly distributed tubules in Model 2 as can be seen in Fig. 12A. However, the addition of a gradient in tubular density in Model 3 significantly decreased the damage volume to below that of Model 1. Wei and Xu [62] found that cellular gradient structures inspired by nacre distribute load better and allow for greater bending deformation before failure. A similar phenomenon occurred in these bioinspired samples where the asymmetric porosity leads to a gradient in effective elastic modulus. Double material samples (Models 4-6) containing reinforced tubules predictably sustained the most damage as samples were embrittled by the addition of the stiffer reinforcing phase. The gradient features, both in tubule density and tubule shape, again led to a decrease in observed damage after impact. The increased soft material in the impact zone blunts the damage while the reinforcement on either side resists the spread of damage. The soft ductile layers further reduced residual damage. Model 8 had the same tubular arrangement as Model 6 but included soft ductile layers. This combination of tubular density and shape gradient alongside ductile lamellae led to the lowest damage volume of the reinforced tubules, providing a positive optimization of stiffness and damage reduction.

A closer look at the segmented damage volume itself revealed how each sample failed under impact. Fig. 12B shows microCT images of the back face of impacted models as well as extracted subvolumes of the damage in each model. The damage volume of Model 1 forms a cylinder near the impact surface before spreading into a conical shape with very smooth fracture surfaces. The tubular features of Models 2 and 3 create more asymmetric damage in the samples as cracks “reach” for tubules that are farther away from the impact zone. This leads to delocalization of damage. In Model 2, cracks extend out from the damage zone before terminating at hollow tubules. In Model 3, the fracture is controlled by the tubular density gradient. Damage occurs preferentially on the more densely porous side of the sample. The unreinforced tubules near the impact zone act as flaws, initiating cracks, while those farther away act as crack arresters; with so many densely packed tubules the crack path is constricted and does not extend past the first row of tubules adjacent to the impact. On the less dense side of the model, fractures behave similarly to those in Model 2, traveling through the matrix towards nearby tubules. Much like the damage mechanisms observed in the horse hoof [3,9,12], this arrangement allows the samples to control the crack propagation.

Fig. 12A shows that Model 2 sustains more damage than Model 1 while Model 3 experiences noticeably less. This is a result of the gradient in density. With tubules near the impact zone acting as crack initiators, the uniform distribution of tubules leads to an increase in damage relative to the neat, featureless samples. The benefits of cracks arrested by distant tubules are outweighed by tubules near the impact zone weakening the material. Mirkhalaf et al. [44] observed a similar phenomenon in glass, noting that when intentional crack deflecting flaws were concentrated too densely they could significantly reduce a material’s overall toughness rather than enhancing it. Meanwhile samples with a gradient in tubules get the benefit of tubule crack arresters while there are fewer tubules near the impact zone to act as crack initiators. Previous authors have postulated about the role of the gradient in tubule density and shape within the hoof. Kasapi and Gosline [9,12] suggest that the denser tubules near the exterior are meant to act as an initial barrier for cracks propagating inward from the outer wall of the hoof, to resist bending, or to provide increased stiffness near the wall’s exterior surface. Our results suggest that this design is meant to incorporate crack arresters near the edges

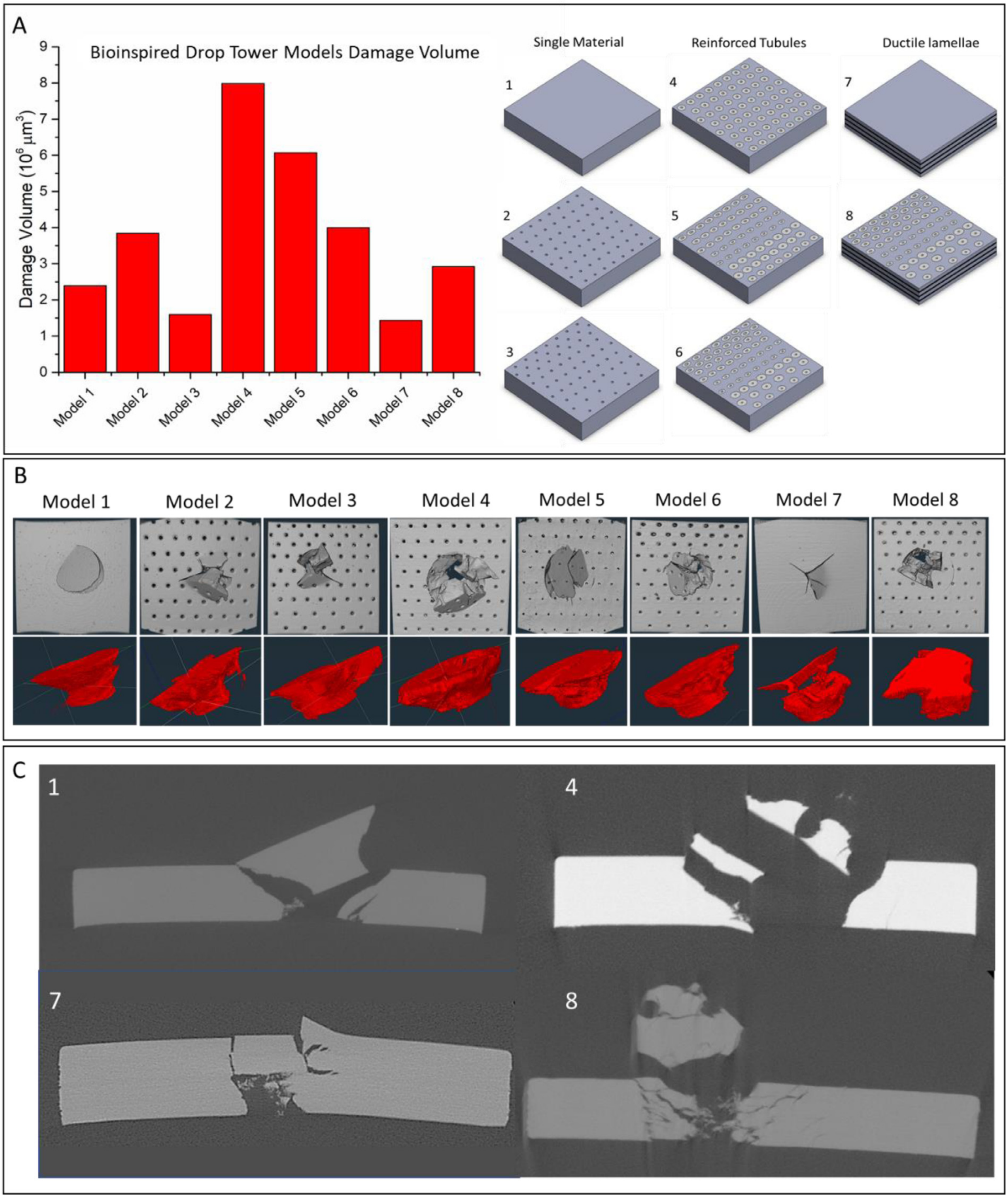

Fig. 12. A) Damage volume after drop tower testing for each of the bioinspired samples, B) Visualizations of the damage volume for each model showing how the different arrangements control crack propagation, and C) Orthogonal slices through the damage zone of four different samples showing the different crack propagation mechanisms.

of the material, which prevent cracks from propagating entirely through the material, causing complete failure. Instead, the damage is localized in the middle of the sample where the tubules are least dense. This is supported by drop tower tests on the hoof itself, where damage to hydrated samples was contained in the central portion of the sample. In the hoof, this corresponds to the mid-wall where Kasapi and Gosline [9,12] identified fiber orientation-related crack deflection mechanisms during non-impact tests that direct damage away from living tissue at the hoof's interior. This observation suggests that if damage occurs from impact *in-vivo* in the hoof, it is contained in the mid-wall by the tubular arrangement while further propagation of these cracks from quasi-static loading (say walking or standing on the hoof) will be redirected towards the exterior.

Model 4 sustained the most damage of any design. Unlike Model 1, damage in Model 4 immediately began to spread into a conical damage shape starting at the impacted surface. In Models 5 and 6, the initial cylindrical shape near the impact surface was once again observed. This is likely the result of having less stiff reinforcement near the impact zone. However, a notable feature of the damage volume for these two models is their jagged fracture surfaces. The denser reinforcement on either side of the impact restricted the spread of damage and deflected fracture interfaces. In some of the tubules near the damage front microcracks were observed in the tubule reinforcement but were arrested at the tubule-matrix interface. Furthermore, the reinforcement reduced the number of cracks traveling through the matrix, resulting in more symmetric, localized damage. The use of tubular gradients is likely meant to strike a balance between stiffness and impact resistance. Without sacrificing the amount of reinforcement, the hoof can improve its impact resistance over uniformly distributed tubules features with this arrangement. In Models 7 and 8, the soft lamellae dampened the impact and absorbed energy via delamination. The back face of Model 7 exhibited very little damage other than a few cracks. The segmented damage volume shows that the conical damage was arrested at one of the lamellar interfaces and only narrow cracks were able to penetrate to the bottom of the sample. The tubular gradient once again controlled the damage volume seen in Model 8, with irregular, asymmetric fracture patterns that indicate deflection at tubular interfaces. Fig. 12C shows a cross-section of the internal cracking of Model 8 compared to Models 1, 4 and 7. In Models 1 and 4, relatively little microcracking was observed, with most damage concentrated in the conical shape directly below the impact. In Model 7, several horizontal cracks were observed along the soft-hard lamellar interfaces, with some fiber bridging occurring. In Model 8, many horizontal cracks initiated along the lamellar interfaces and radiated outward.

These tests show that many beneficial failure mechanisms identified in the horse hoof wall can be translated into engineered materials by utilizing bioinspired designs. These include deflections at tubular interfaces, tubular gradients as a means of fracture control, and soft lamellar arrangements dampening impacts and delocalizing damage. However, there are features unique to the hoof that are very challenging to replicate. For example, the hierarchically intertwined fibers of the tubular reinforcement found in the hoof would be very difficult to recreate in a man-made structure. Also, certain failure mechanisms commonly observed in post-impacted hoof wall, such as tubule pullout, were not observed in the bioinspired designs. This could be a result of the scale difference between the biological structures and the 3D printed designs or from differences in sub-tubular scale features and properties.

3.4.2. Quasistatic tests (compact tension)

Computer aided design depictions of the compact tension models are shown in Fig. 13A. The compact tension models are based on the same models that were used for the drop tower designs. Two extra models were introduced to compare featureless designs of just the stiff reinforcing tubular material and a model which has uniformly distributed tubules with an elliptical reinforcing region. For the latter, a shape ratio of 1.62 was chosen as this correlated to the most extreme elliptical tubules observed in the hoof by Kasapi et al. [9].

All fractured samples are shown in Fig. 13B. Models 1-3, with no reinforcement, maintained a relatively straight crack through the sample while Models 4-7, with tubular reinforcement composed of the stiffer VeroClear phase, experienced torturous crack deflection around tubular regions. Particularly in Models 2 and 3, the crack passes directly through the medullary cavities where the cavities act as flaws. Resulting load versus displacement curves provide insight for the performance of the models. The averages for each model were plotted in Fig. 13C and D for control Models 1a and 1b and Models 1a, 2-7 respectively. For the control models, Model 1a maintained a smooth curve representing the expected ductile nature of the printed material. The stiff Model 1b experienced brittle fracture almost immediately after the experiment began. Models 2 and 3, with no reinforced cavities, rendered curves with smaller maximum loadings as the crack propagated through the cavities. The maximum loads and overall curves for Models 4-7 were greater than for Models 1a, and 2, and 3. The introduction of cavities into the bioinspired hoof structure dramatically decreased the mechanical toughness of the samples, as noticed by comparing Model 1a to Models 2 and 3, since the cavities act as flaws guiding the crack relentlessly through the material. This observation supports Kasapi and Gosline's [63] theory that the hollow cavities are either a manufacturing constraint, meant to reduce the weight of the hoof, or resist co-operative buckling of the individual reinforcing elements under longitudinal compression rather than as a means of improving fracture toughness.

The reinforced tubular structure caused crack deflection that led to torturous crack paths, which is attributed to its high energy absorbing behavior. Furthermore, the density gradient feature in combination with the reinforced tubular structure exhibited consistent fracture control properties due to the congestion of tubules near the crack tip and further implied crack path manipulation. Through video correlation, the ridges in the curves of Models 2-7 were caused by a tubule or cavity acting as obstacle interface for the propagating crack. When the specimen's crack path was halted by a tubule in the crack path, a ridge was formed in the curve as it required an extra amount of load to deviate around or through the tubule. This hypothesis is reinforced by the curve in Model 1a and 1b, with no tubular features, maintaining a smooth curve throughout.

The energy absorbed by each model is compared in Fig. 13E. Models 4-7 rendered energy absorption that was nearly two times larger than the control Model 1a, nearly four times larger than Models 2 and 3, and nearly six times larger than Model 1b, the stiff tubular material alone. While the reinforced tubular structure appeared to have aided in increasing energy absorption, another notable result was regarding fracture control. Samples of Model 7 had very similar curves and took the same crack path in all three trials generating significantly similar curves as shown in Fig. 13F. On Fig. 13E, intervals marked on each bar represent standard deviation with Model 7 rendering the smallest standard deviation out of the multiple material models, trailing behind Models 2 and 3 where their lower standard deviations are most likely due to the nonreinforced cavities guiding the crack path. Model 7's consistency could be due to the density gradient feature. By congesting the number of tubules towards the front of the model, the crack was guided by the reinforced tubules down a particular ideal path. Model 7, which is most like the hoof, did not absorb as much energy as Models 4-6 did. However, this may indicate a tradeoff relationship between fracture control and toughness of a structure. The very slight decrease in energy absorption may be a small price to pay for unique fracture control properties.

Lastly, crack deflection was further quantified by finding the initial angle deflection, the angle measured from crack initiation to 50% displacement of the specimen as noted in Fig. 14A. Average calculated initial angle deflection for each model is listed Fig. 14B. Larger angles imply greater crack deflection occurring and propagating through a more torturous path rather than a straight line. Models 4-7 had overall greater angle deflection, implying that crack deflection was highly present during fracture due to the reinforced tubular structure. Likewise, the average crack length of each Model was measured and displayed in Fig. 14C and the average crack length was greater by about 3 mm for Models 4-7 than Models 1-3, which likewise implies greater crack deflection. Crack deflection can also be generally attributed to the increased energy absorbing properties of the tubular structure. While each of the models with reinforced tubules had relatively similar crack lengths, the model with all elliptical tubules had the longest crack

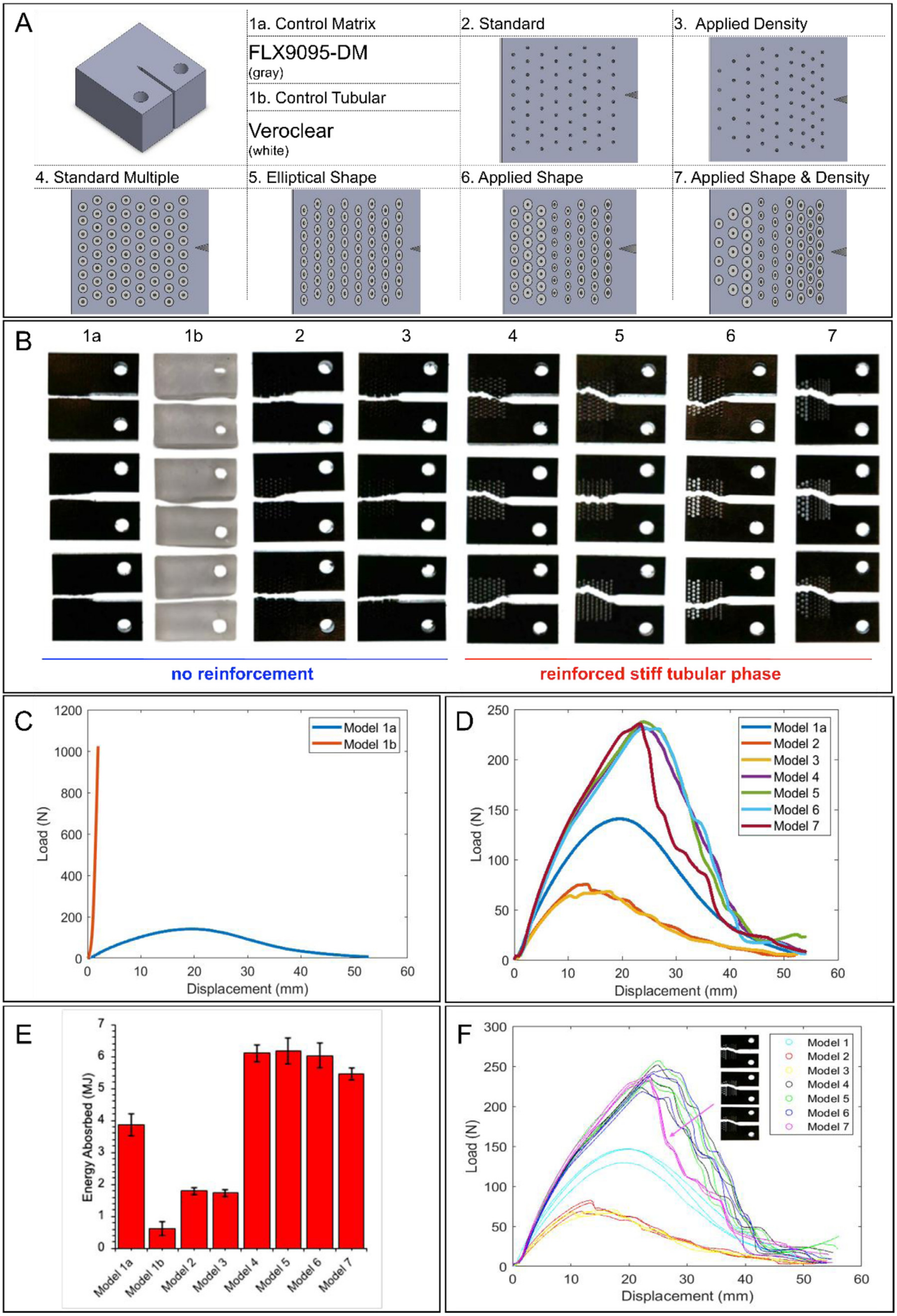

Fig. 13. A) Computer aided design models of the compact tension samples. B) Post-fracture image of samples. C) Averaged Load (N) vs. Displacement (mm) of Model 1a and 1b. D) Averaged Load (N) vs. Displacement (mm) of Models 1a, 2-7. E) Bar graph of average Energy Absorbed (MJ) for each model with intervals indicating standard deviation. F) All trials plotted in Load (N) vs. Displacement (mm) for Models 1a, 2-7.

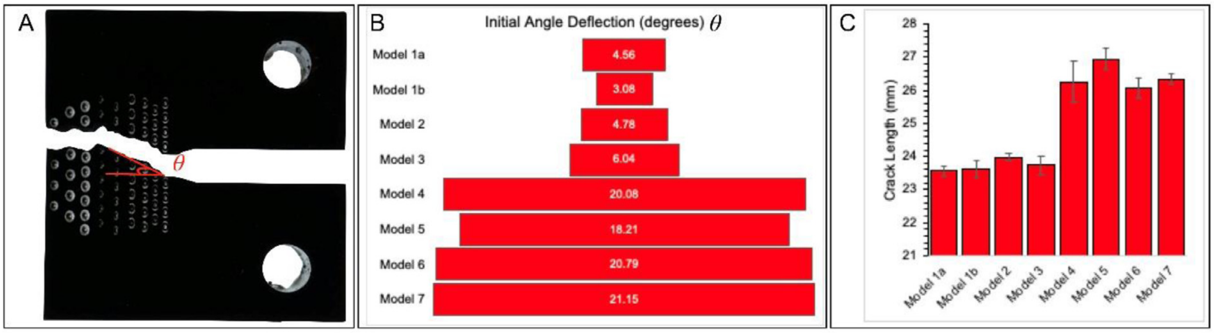

Fig. 14. A) Initial Angle Deflection indicated on a fractured sample. B) Funnel graph of initial angle of deflection. C) Average Crack Length (mm) measured per each Model from crack start to end of sample.

length, likely due to the larger deflections required to circumvent the longer perimeter of each ellipse. Kasapi and Gosline [9] suggest that the elliptical nature of the tubules is meant to withstand bending or to prevent tubules from collapsing due to circumferential stresses that arise at the edge of the hoof wall. However, the elliptical tubules may also play a beneficial role in resisting the propagation of orthogonal “quarter-cracks” (an issue in distorted hoof capsules where cracks run parallel to the tubules and can cause lameness and infection [64]) by increasing crack tortuosity at the exterior portion of the hoof. Meanwhile, the large, circular tubules in the interior, further from the location that cracks would be expected to initiate, would be better able to resist longitudinal bending and buckling.

4. Conclusions

The load bearing horse hoof wall has evolved a unique design and properties to survive the demands placed on it *in-vivo*. Previous authors have identified this evolutionary marvel as a remarkable material for engineers to learn from, yet knowledge gaps surrounding the hoof wall’s architecture and its relation to the compressive, viscoelastic, and impact behavior of the wall remained. This study reaches significant conclusions that expand our understanding of the structure and mechanical response of the horse hoof wall:

1. Several features in the hoof wall were quantified and characterized using microCT and SEM. Results from previous studies on porosity, tubule density, and tubule cross-section were confirmed while new values such as average tubule bridge width and bridge density are reported for the first time.
2. Drop tower tests suggested that these previously unexplored features play a mechanical role in the hoof wall, stabilizing the hollow medullary cavity, and being the first part of the tubule to crack during an impact scenario.
3. Other fracture mechanisms observed by previous authors were noted after drop tower tests such as tubule pullout and deflections at the tubular and lamellar interfaces. However, our impact fractogaphy results contradict the analysis of tensile fracture presented by Kasapi and Gosline [9,12] and Bertram and Gosline [6,7] who suggest that cracks nearly always prefer to propagate along the intertubular IF orientation. While the intertubular fiber orientation leads to a slight deviation in crack path during impact, the tubules dominate the fracture pattern, particularly at lower impact speeds. At higher impact energies, cracks more commonly propagate between the intertubular lamellae, but fractures still traveled through the sample along the tubular axis.
4. A hierarchy of fibers were also identified within the hoof wall. During cracking these fibers play a key role by intertwining the tubular reinforcement with the matrix. These observations reveal unique mechanisms that are not normally observed in synthetic composites such as tubule bridging or arresting where tubules extrinsically toughen the hoof by spanning crack interfaces or by arresting propagation at the tip altogether. The fibrous entanglement with the matrix also strengthens the interphase zone of the composite, requiring more energy to induce delamination or pullout of the reinforcing phase since fibers need to be ruptured to do so. This architecture is challenging to replicate but offers an ingenious design motif to improve composite materials, which can be limited by the ability of the reinforcement to adhere to the matrix.
5. To test the role of hydration on the impact resistance of the hoof, drop tower tests were performed at two different hydration states. The samples equilibrated at 50% relative humidity showed minimal damage with most samples exhibiting a small dimple at the impact zone. All samples in the 25% relative humidity environment developed cracks with most samples cracking through the thickness of the sample in multiple places.
6. Quasi-static compression was used to build a better understanding of the ductile-brittle transition in the hoof. Samples hydrated to 30% water content exhibited a ductile behavior across all strain rates (10^{-4} s^{-1}-10^{0} s^{-1}) while samples hydrated to 10% water content consistently showed brittle behavior dependent on catastrophic events that began around 0.15 strain. Young’s moduli and strain rate sensitivity were also determined and were in range with those of other keratinous materials.
7. Relaxation tests revealed that samples hydrated to 20% water content dissipated more stress, faster than samples hydrated to 10% or 30% water content. In the hoof, this is a very useful trait, since there is a hydration gradient, and therefore stiffness gradient, that exists through the hoof’s thickness leading to loading differentials and internal stresses between the interior and exterior. Twenty percent water content by weight seems to be an ideal optimization for the hoof’s exterior that maximizes relaxation speed (reducing internal stresses) while increasing stiffness.
8. Fitting the relaxation data to a Maxwell-Weichert model using a Prony series showed that this quicker relaxation was due to the hoof’s mesostructural features. Further, the hoof’s relaxation due to mesofeatures is faster than that of other keratinous materials, such as hair, where being able to quickly recover from loading may not be as evolutionarily important.

To show that the benefits of the hoof wall’s design can be translated to engineered materials, bioinspired designs were fabricated using a multi-material 3D printer to replicate the tubular, lamellar, and gradient arrangements found in the hoof. These specimens were subjected to drop tower and fracture toughness tests which showed the interaction of matrix and tubules:

1. Drop tower tests on single material samples showed that tubules act as both crack arresters as well as crack initiators. In samples with uniformly distributed tubule cavities the material weakness introduced by the cavities outweighed the benefits of cavities arresting cracks. With the introduction of a gradient in tubule cavity density, a decrease in damage was observed. This likely results from the fact that fewer tubules are located near the impact zone to act as initiators while more densely packed tubules further from the impact zone continue to arrest crack propagation. The introduction of a more brittle reinforcing phase predictably increased the total damage observed in the samples. However, the application of a gradient again led to a decrease in damage relative to samples with a uniform tubule distribution. This highlights that a gradient in reinforcement density can be used to improve impact resistance without reducing the amount of reinforcement in the material. The addition of soft lamellae further reduced the overall damage of the samples. Much like the drop tower tests performed on hoof samples, impact tests on the 3D printed samples led to crack deflections along the tubular and lamellar interfaces.
2. Compact tension fracture toughness tests on 3D printed samples showed a large increase in crack deflection angle and crack length for samples with reinforcement. While gradient samples showed a slight drop in energy absorbed, they produced predictable fracture patterns with very little deviation in mechanical response between samples.

The present study shows that the hoof contains several unique structure-property relationships that enable it to survive its environmental demands. Its mesostructure improves impact resistance while also allowing it to reduce internal stresses via rapid viscoelastic relaxation. The importance of several architectures such as cavity bridges and reinforcing elements that are physically intertwined with the matrix were identified and these features offer inspiration for future study. Other previously identified aspects of the hoof wall such as tubules, lamellae, and gradient configurations show significant promise as design elements in engineered materials and warrant continued research, particularly as designs to be used in tandem.

Declaration of Competing Interest

The authors declare that they have no known competing financial interests or personal relationships that could have appeared to influence the work reported in this paper.

Acknowledgments

We acknowledge funding from the National Science Foundation Mechanics of Materials and Structures program (Grant numbers 1926353 and 1926361). We thank Eric Bushong and the National Center for Microscopy and Imaging Research for their help in acquiring microCT scans. We also thank Sabine Faulhaber and the NanoEngineering Materials Research Center as well as Nano3 for their help in obtaining SEM images. We would also like to thank Michael Ishida and the Tolley Lab for their assistance in printing bioinspired designs as well as Kiwon Oh and Professor Yu Qiao for their help with impact testing of the printed structures. Finally, the late Professor Joanna McKittrick was an inspiring influence for this project and her contributions were vital to this publication.

References

[1] S.E. Naleway, M.M. Porter, J. McKittrick, M.A. Meyers, Structural design elements in biological materials: application to bioinspiration, Adv. Mater. 27 (2015) 5455–5476, doi:10.1002/adma.201502403.

[2] B.S. Lazarus, A. Velasco-Hogan, T. Gómez-del Río, M.A. Meyers, I. Jasiuk, A review of impact resistant biological and bioinspired materials and structures, J. Mater. Res. Technol. 9 (2020) 15705–15738, doi:10.1016/j.jmrt.2020.10.062.

[3] M.A. Kasapi, J.M. Gosline, Micromechanics of the equine hoof wall: optimizing crack control and material stiffness through modulation of the properties of keratin, J. Exp. Biol. 202 (1999) 337–391.

[4] J.D. Reilly, D.F. Cottrell, R.J. Martin, D. Cuddeford, Tubule density in equine hoof horn, Biomimetics 4 (1996) 23–35 https://www.researchgate.net/publication/251565789.

[5] D.H. Leach, The Structure and Function of the Equine Hoof Wall (PhD Thesis), University of Saskatchewan, 1980.

[6] J.E. Bertram, J.M. Gosline, Functional design of horse hoof keratin: the modulation of mechanical properties through hydration effects, J. Exp. Biol. 130 (1987) 121–136.

[7] J.E. Bertram, J.M. Gosline, Fracture toughness design in horse hoof keratin, J. Exp. Biol. 125 (1986) 29–47.

[8] W. Huang, N.A. Yaraghi, W. Yang, A. Velazquez-Olivera, Z. Li, R.O. Ritchie, D. Kisailus, S.M. Stover, J. McKittrick, A natural energy absorbent polymer composite: the equine hoof wall, Acta Biomater. 90 (2019) 267–277, doi:10.1016/j.actbio.2019.04.003.

[9] M.A. Kasapi, J.M. Gosline, Design complexity and fracture control in the equine hoof wall, J. Exp. Biol. 200 (1997) 1639–1659.

[10] J.E. Douglas, C. Mittal, J.J. Thomason, J.C. Jofriet, The modulus of elasticity of equine hoof wall: implications for the mechanical function of the hoof, J. Exp. Biol. 199 (1996) 1829–1836.

[11] S.N. Collins, B.C. Cope, L. Hopegood, R.J. Latham, R.G. Linford, J.D. Reilly, Stiffness as a function of moisture content in natural materials: characterisation of hoof horn samples, J. Mater. Sci. 33 (1998) 5185–5191, doi:10.1023/A:1004479803611.

[12] M.A. Kasapi, J.M. Gosline, Strain-rate-dependent mechanical properties of the equine hoof wall, J. Exp. Biol. 199 (1996) 1133–1146.

[13] B.W. Li, H.P. Zhao, X.Q. Feng, W.W. Guo, S.C. Shan, Experimental study on the mechanical properties of the horn sheaths from cattle, J. Exp. Biol. 213 (2010) 479–486, doi:10.1242/jeb.035428.

[14] R.D. Fraser, T.P. Macrae, Molecular structure and mechanical properties of keratins, Symp. Soc. Exp. Biol. 34 (1980) 211–246 http://europepmc.org/abstract/MED/6166998.

[15] D. Zhang, D.D. Arola, R.K. Reprogel, W. Zheng, U. Tasch, R.M. Dyer, A method for characterizing the mechanical behaviour of hoof horn, J. Mater. Sci. 42 (2007) 1108–1115, doi:10.1007/s10853-006-0614-6.

[16] W. Huang, A. Zaheri, W. Yang, D. Kisailus, R.O. Ritchie, H. Espinosa, J. McKittrick, How water can affect keratin: hydration-driven recovery of bighorn sheep (Ovis Canadensis) horns, Adv. Funct. Mater. 29 (2019) 1901077, doi:10.1002/adfm.201901077.

[17] D.A. Greenberg, D.S. Fudge, Regulation of hard α-keratin mechanics via control of intermediate filament hydration: matrix squeeze revisited, Proc. R. Soc. B Biol. Sci. 280 (2013) 20122158, doi:10.1098/rspb.2012.2158.

[18] B. Lazarus, C. Chadha, A. Velasco-Hogan, J.D.V Barbosa, I. Jasiuk, M.A. Meyers, Engineering with keratin: a functional material and a source of bioinspiration, IScience (2021) 102798, doi:10.1016/j.isci.2021.102798.

[19] Z.Q. Liu, D. Jiao, Z.Y. Weng, Z.F. Zhang, Structure and mechanical behaviors of protective armored pangolin scales and effects of hydration and orientation, J. Mech. Behav. Biomed. Mater. 56 (2016) 165–174, doi:10.1016/j.jmbbm.2015.11.013.

[20] B. Wang, W. Yang, V.R. Sherman, M.A. Meyers, Pangolin armor: overlapping, structure, and mechanical properties of the keratinous scales, Acta Biomater. 41 (2016) 60–74, doi:10.1016/j.actbio.2016.05.028.

[21] P. Fortier, S. Suei, L. Kreplak, Nanoscale strain-hardening of keratin fibres, PLoS One 7 (2012) e41814, doi:10.1371/journal.pone.0041814.

[22] L. Kreplak, J. Doucet, F. Briki, Unraveling double stranded α-helical coiled coils: an x-ray diffraction study on hard α-keratin fibers, Biopolymers 58 (2001) 526–533, doi:10.1002/1097-0282(20010415)58:5⟨526::AID-BIP1028⟩3.0.CO;2-L.

[23] L. Kreplak, J. Doucet, P. Dumas, F. Briki, New aspects of the α-helix to β-sheet transition in stretched hard α-keratin fibers, Biophys. J. 87 (2004) 640–647, doi:10.1529/biophysj.103.036749.

[24] D.S. Fudge, K.H. Gardner, V.T. Forsyth, C. Riekel, J.M. Gosline, The mechanical properties of hydrated intermediate filaments: insights from hagfish slime threads, Biophys. J. 85 (2003) 2015–2027, doi:10.1016/S0006-3495(03)74629-3.

[25] C. Rice, K.T. Tan, Horse hoof inspired biomimetic structure for improved damage tolerance and crack diversion, Compos. Struct. 220 (2019) 362–370, doi:10.1016/j.compstruct.2019.04.009.

[26] B. Wang, B. Zhou, X. Zhang, A high toughness and light weight armor structure bioinspired design based on a bovine hoof wall, Mater. Lett. 264 (2020) 127296, doi:10.1016/j.matlet.2020.127296.

[27] W. Huang, Impact Resistant and Energy Absorbent Natural Keratin Materials: Horns and Hooves (PhD Thesis), University of California San Diego, 2018.

[28] W. Ma, S. Xie, Z. Li, Mechanical performance of bio-inspired corrugated tubes with varying vertex configurations, Int. J. Mech. Sci. 172 (2020) 105399, doi:10.1016/j.ijmecsci.2019.105399.

[29] J. Schindelin, I. Arganda-Carreras, E. Frise, V. Kaynig, M. Longair, T. Pietzsch, S. Preibisch, C. Rueden, S. Saalfeld, B. Schmid, J.-Y. Tinevez, D.J. White, V. Hartenstein, K. Eliceiri, P. Tomancak, A. Cardona, Fiji: an open-source platform for biological-image analysis, Nat. Methods 9 (2012) 676–682, doi:10.1038/nmeth.2019.

[30] D. Legland, I. Arganda-Carreras, P. Andrey, MorphoLibJ: integrated library and plugins for mathematical morphology with ImageJ, Bioinformatics 32 (2016) 3532–3534, doi:10.1093/bioinformatics/btw413.

[31] J. Ollion, J. Cochennec, F. Loll, C. Escudé, T. Boudier, TANGO: a generic tool for high-throughput 3D image analysis for studying nuclear organization, Bioinformatics 29 (2013) 1840–1841, doi:10.1093/bioinformatics/btt276.

[32] S. Lee, E.E. Novitskaya, B. Reynante, J. Vasquez, R. Urbaniak, T. Takahashi, E. Woolley, L. Tombolato, P.Y. Chen, J. McKittrick, Impact testing of structural biological materials, Mater. Sci. Eng. C 31 (2011) 730–739, doi:10.1016/j.msec.2010.10.017.

[33] B. Wang, T.N. Sullivan, A. Pissarenko, A. Zaheri, H.D. Espinosa, M.A. Meyers, Lessons from the Ocean: whale baleen fracture resistance, Adv. Mater. 31 (2019) 1804574, doi:10.1002/adma.201804574.

[34] K.L. Johnson, M.W. Trim, D.K. Francis, W.R. Whittington, J.A. Miller, C.E. Bennett, M.F. Horstemeyer, Moisture, anisotropy, stress state, and strain rate effects on bighorn sheep horn keratin mechanical properties, Acta Biomater. 48 (2017) 300–308, doi:10.1016/j.actbio.2016.10.033.

[35] H. Quan, D. Kisailus, M.A. Meyers, Hydration-induced reversible deformation of biological materials, Nat. Rev. Mater. 6 (2021) 264–283, doi:10.1038/s41578-020-00251-2.

[36] B. Wang, W. Yang, J. McKittrick, M.A. Meyers, Keratin: structure, mechanical properties, occurrence in biological organisms, and efforts at bioinspiration, Prog. Mater. Sci. 76 (2016) 229–318.

[37] Y. Seki, B. Kad, D. Benson, M.A. Meyers, The toucan beak: structure and mechanical response, Mater. Sci. Eng. C 26 (2006) 1412–1420, doi:10.1016/j.msec.2005.08.025.

[38] T.N. Sullivan, Y. Zhang, P.D. Zavattieri, M.A. Meyers, Hydration-induced shape and strength recovery of the feather, Adv. Funct. Mater. 28 (2018) 1801250, doi:10.1002/adfm.201801250.

[39] Y. Yu, W. Yang, M. André Meyers, Viscoelastic properties of α-keratin fibers in hair, Acta Biomater. 64 (2017) 15–28, doi:10.1016/j.actbio.2017.09.012.

[40] S. Breakspear, B. Noecker, C. Popescu, Relevance and evaluation of hydrogen and disulfide bond contribution to the mechanics of hard α-keratin fibers, J. Phys. Chem. B 123 (2019) 4505–4511, doi:10.1021/acs.jpcb.9b01690.

[41] D.S. Fudge, J.M. Gosline, Molecular design of the α-keratin composite: insights from a matrix-free model, hagfish slime threads, Proc. R. Soc. B Biol. Sci. 271 (2003) 291–299, doi:10.1098/rspb.2003.2591.

[42] H.M. Clayton, S.J. Hobbs, A review of biomechanical gait classification with reference to collected trot, passage and piaffe in dressage horses, Anim. Open Access J. MDPI 9 (2019) 763, doi:10.3390/ani9100763.

[43] B.Y.J.J. Thomason, Surface strain on the equine hoof wall *in vivo*: implications for the material design and functional morphology of the wall, J. Exp. Biol. 166 (1992) 145–168.

[44] M. Mirkhalaf, A.K. Dastjerdi, F. Barthelat, Overcoming the brittleness of glass through bio-inspiration and micro-architecture, Nat. Commun. 5 (2014) 3166, doi:10.1038/ncomms4166.

[45] R.O. Ritchie, The conflicts between strength and toughness, Nat. Mater. 10 (2011) 817–822, doi:10.1038/nmat3115.

[46] N.C. Huang, X.Y. Liu, Debonding and fiber pull-out in reinforced composites, Theor. Appl. Fract. Mech. 21 (1994) 157–176, doi:10.1016/0167-8442(94)90031-0.

[47] R. Rizvi, A. Anwer, G. Fernie, T. Dutta, H. Naguib, Multifunctional textured surfaces with enhanced friction and hydrophobic behaviors produced by fiber debonding and pullout, ACS Appl. Mater. Interfaces 8 (2016) 29818–29826, doi:10.1021/acsami.6b11497.

[48] A. Naaman, G. Namur, J. Alwan, H. Najm, Fiber pullout and bond slip. II: experimental validation, J. Struct. Eng. 117 (1991) 2791–2800, doi:10.1061/(ASCE)0733-9445(1991)117:9(2791).

[49] A. Naaman, G. Namur, J. Alwan, H. Najm, Fiber pullout and bond slip. I: analytical study, J. Struct. Eng. 117 (1991) 2769–2790, doi:10.1061/(ASCE)0733-9445(1991)117:9(2769).

[50] A.K. Matsushita, D. Gonzalez, M. Wang, J. Doan, Y. Qiao, J. Mckittrick, Beyond density: mesostructural features of impact resistant wood, Mater. Today Commun. 22 (2020) 100697, doi:10.1016/j.mtcomm.2019.100697.

[51] L. Wang, Y. Cui, Q. Qin, H. Wang, J. Wang, Helical fiber pull-out in biological materials, Acta Mech. Solida Sin. 29 (2016) 245–256, doi:10.1016/S0894-9166(16)30159-8.

[52] W.J. Cantwell, J. Morton, The impact resistance of composite materials - a review, Composites 22 (1991) 347–362, doi:10.1016/0010-4361(91)90549-V.

[53] P.W.R. Beaumont, in: Fracture Mechanisms in Fibrous Composites, Pergamon, 1979, pp. 211–233, doi:10.1016/B978-0-08-024766-3.50012-4.

[54] Q. Wu, Q. Wan, Q. Liu, J. He, R. Zhao, X. Yang, F. Wang, J. Guo, J. Zhu, Synergistic strengthening and toughening the interphase of composites by constructing alternating “rigid-and-soft” structure on carbon fiber surface, Adv. Mater. Interfaces 6 (2019) 1900970, doi:10.1002/admi.201900970.

[55] N.A. Isitman, M. Aykol, C. Kaynak, Nanoclay assisted strengthening of the fiber/matrix interface in functionally filled polyamide 6 composites, Compos. Struct. 92 (2010) 2181–2186, doi:10.1016/j.compstruct.2009.09.007.

[56] O. Zabihi, M. Ahmadi, Q. Li, S. Shafei, M.G. Huson, M. Naebe, Carbon fibre surface modification using functionalized nanoclay: a hierarchical interphase for fibre-reinforced polymer composites, Compos. Sci. Technol. 148 (2017) 49–58, doi:10.1016/j.compscitech.2017.05.013.

[57] R. Li, N. Lachman, P. Florin, H.D. Wagner, B.L. Wardle, Hierarchical carbon nanotube carbon fiber unidirectional composites with preserved tensile and interfacial properties, Compos. Sci. Technol. 117 (2015) 139–145, doi:10.1016/j.compscitech.2015.04.014.

[58] S. Hong, M. Minary-Jolandan, M. Naraghi, Controlling the wettability and adhesion of carbon fibers with polymer interfaces via grafted nanofibers, Compos. Sci. Technol. 117 (2015) 130–138, doi:10.1016/j.compscitech.2015.06.008.

[59] S. Jiang, Q. Li, Y. Zhao, J. Wang, M. Kang, Effect of surface silanization of carbon fiber on mechanical properties of carbon fiber reinforced polyurethane composites, Compos. Sci. Technol. 110 (2015) 87–94, doi:10.1016/j.compscitech.2015.01.022.

[60] A. Gargano, K. Pingkarawat, V.L. Pickerd, M.E. Ibrahim, A.P. Mouritz, Effect of fibre-matrix interfacial strength on the explosive blast resistance of carbon fibre laminates, Compos. Sci. Technol. 138 (2017) 68–79, doi:10.1016/j.compscitech.2016.11.009.

[61] F. Gnädinger, P. Middendorf, B. Fox, Interfacial shear strength studies of experimental carbon fibres, novel thermosetting polyurethane and epoxy matrices and bespoke sizing agents, Compos. Sci. Technol. 133 (2016) 104–110, doi:10.1016/j.compscitech.2016.07.029.

[62] Z. Wei, X. Xu, Gradient design of bio-inspired nacre-like composites for improved impact resistance, Compos. Part B Eng. 215 (2021) 108830, doi:10.1016/j.compositesb.2021.108830.

[63] M.A. Kasapi, J.M. Gosline, Exploring the possible functions of equine hoof wall tubules, Equine Vet. J. 30 (1998) 10–14, doi:10.1111/j.2042-3306.1998.tb05116.x.

[64] S.E. O’Grady, How to manage a quarter crack, Annu. Conv. AAEP (2010) 141–147.